

An improved threshold dynamics method for wetting dynamics



Dong Wang^a, Xiao-Ping Wang^{b,*}, Xianmin Xu^{c,d}

^a Department of Mathematics, University of Utah, Salt Lake City, UT, 84112, USA

^b Department of Mathematics, The Hong Kong University of Science and Technology, Hong Kong, China

^c LSEC, Institute of Computational Mathematics and Scientific/Engineering Computing, NCMIS, Academy of Mathematics and Systems Science, Chinese Academy of Sciences, Beijing 100190, China

^d School of Mathematical Sciences, University of Chinese Academy of Sciences, Beijing 100049, China

ARTICLE INFO

Article history:

Received 26 August 2018

Received in revised form 15 April 2019

Accepted 15 April 2019

Available online 30 April 2019

Keywords:

Threshold dynamics method

Wetting

Contact point

Young's angle

Gaussian kernel

ABSTRACT

We propose a modified threshold dynamics method for wetting dynamics, which significantly improves the behavior near the contact line compared to the previous method (J. Comput. Phys. 330 (2017) 510–528). The new method is also based on minimizing the functional consisting of weighted interface areas over an extended domain including the solid phase. However, each interface area is approximated by the Lyapunov functional with a different Gaussian kernel. We show that a correct contact angle (Young's angle) is obtained in the leading order by choosing correct Gaussian kernel variances. We also show the Gamma convergence of the functional to the total surface energy. The method is simple, unconditionally stable with $O(N \log N)$ computational complexity per time step and is not sensitive to the inhomogeneity or roughness of the solid surface. It is also shown that the dynamics of the contact point is consistent with the dynamics of the interface away from the contact point. Numerical examples have shown significant improvements in the accuracy of the contact angle and the hysteresis behavior of the contact angle.

© 2019 Elsevier Inc. All rights reserved.

1. Introduction

Wetting describes how a liquid drop spreads on a solid surface. The study of wetting is of critical importance for many applications and has attracted much interest in the physics and applied mathematics communities [2,11,16,35,50]. The equilibrium configuration of the liquid drop can be obtained by minimizing the total interface energy:

$$\mathcal{E} = \gamma_{LV} |\Sigma_{LV}| + \gamma_{SL} |\Sigma_{SL}| + \gamma_{SV} |\Sigma_{SV}| \quad (1)$$

where γ_{SV} , γ_{SL} and γ_{LV} are the solid-vapor, solid-liquid and liquid-vapor surface energy densities, respectively and $|\Sigma_{SV}|$, $|\Sigma_{SL}|$ and $|\Sigma_{LV}|$ are the corresponding interface areas. When the solid surface is homogeneous, the contact angle for a static drop is given by the famous Young's equation:

$$\cos \theta_Y = \frac{\gamma_{SV} - \gamma_{SL}}{\gamma_{LV}}, \quad (2)$$

* Corresponding author.

E-mail addresses: dwang@math.utah.edu (D. Wang), mawang@ust.hk (X.-P. Wang), xmxu@lsec.cc.ac.cn (X. Xu).

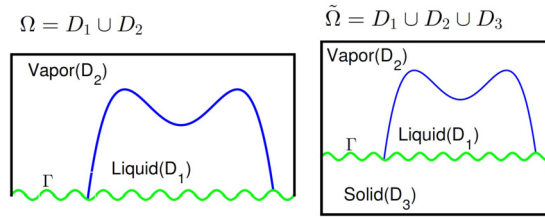


Fig. 1. Left: Original domain $\Omega = D_1 \cup D_2$. Right: Extended computational domain $\tilde{\Omega} = \Omega \cup D_3$.

where θ_Y is the so-called Young’s angle [51]. Analytic solution of the minimization problem of (1) is difficult and the numerical solution is also challenging. There have been many numerical methods proposed for simulating the free interface problem using front-tracking [25,48], level set method [52] or the phase-field method [9,17].

The threshold dynamics method developed by Merriman, Bence, and Osher (MBO) [29] is an efficient numerical method for the motion of the interface driven by the mean curvature. The method alternately diffuses and sharpens characteristic functions of regions and is easy to implement and highly efficient. The MBO method has been shown to converge to the continuous motion by mean curvature [3,5,15,42] when the interface is away from the solid boundary. Esedoglu and Otto [13] generalized this type of method to multiphase flow with arbitrary surface tensions. The method has attracted much attention and becomes very popular due to its simplicity and unconditional stability. It has been subsequently extended to deal with many other applications including the problem of area or volume preserving interface motion [19,21,41,48], image processing [12,28,45], problems of anisotropic interface motions [4,10,31,39], generating quad mesh [43], and foam bubble problems [44]. Various algorithms and rigorous error analysis have been carried out to refine and extend the original MBO method and related methods for the aforementioned problems (see, for example, [14,18,26,30,37,38,40]). Some mesh free methods are also considered to accelerate this type of method [20] based on non-uniform fast Fourier transform (NUFFT) [8,24]. Laux et al. [22,23] rigorously proved the convergence of the method proposed in [13]. Recently, a generalized target-valued diffusion generated method was studied in [33,34,46,47].

In [49], we proposed an efficient threshold dynamics method for the wetting and interface motion on the rough solid surface. The domain is extended to include the solid phase as the third phase and the method is based on the minimization of the approximate energy to (1) (as $h \rightarrow 0$)

$$\mathcal{E}^h(\chi_{D_1}, \chi_{D_2}) = \frac{\gamma_{LV}\sqrt{\pi}}{\sqrt{h}} \int_{\tilde{\Omega}} \chi_{D_1} G_h * \chi_{D_2} \, d\mathbf{x} + \frac{\gamma_{SL}\sqrt{\pi}}{\sqrt{h}} \int_{\tilde{\Omega}} \chi_{D_1} G_h * \chi_{D_3} \, d\mathbf{x} + \frac{\gamma_{SV}\sqrt{\pi}}{\sqrt{h}} \int_{\tilde{\Omega}} \chi_{D_2} G_h * \chi_{D_3} \, d\mathbf{x}, \tag{3}$$

where

$$G_h(\mathbf{x}) = \frac{1}{(4\pi h)^{n/2}} \exp\left(-\frac{|\mathbf{x}|^2}{4h}\right) \tag{4}$$

is the Gaussian kernel and χ_{D_1} and χ_{D_2} are characteristic functions of domain D_1, D_2 in Fig. 1. An efficient iterative algorithm is then designed to find the minimizer of (3) (with volume constraints on D_1 and D_2). The method is simple, efficient, unconditionally stable and insensitive to the inhomogeneity of the solid surface. However, numerical experiments in [49] have shown that, although the apparent (macroscopic) contact angle satisfies the Young’s equation, the microscopic contact angle at the contact point deviates from the correct Young’s angle. There seems to be a boundary layer on the solid surface around the contact points.

In this paper, we show that the method can be improved by using heat kernel with different variances for different surface energy terms in (3), i.e.,

$$\mathcal{E}^{h_1, h_2}(\chi_{D_1}, \chi_{D_2}) = \frac{\gamma_{LV}\sqrt{\pi}}{\sqrt{h_1}} \int_{\tilde{\Omega}} \chi_{D_1} G_{h_1} * \chi_{D_2} \, d\mathbf{x} + \frac{\gamma_{SL}\sqrt{\pi}}{\sqrt{h_2}} \int_{\tilde{\Omega}} \chi_{D_1} G_{h_2} * \chi_{D_3} \, d\mathbf{x} + \frac{\gamma_{SV}\sqrt{\pi}}{\sqrt{h_2}} \int_{\tilde{\Omega}} \chi_{D_2} G_{h_2} * \chi_{D_3} \, d\mathbf{x}, \tag{5}$$

where we use h_1 for approximating the liquid-vapor interface energy and h_2 for approximating the solid-liquid and the solid-vapor interface energy. We perform asymptotic analysis and show that, to remove the boundary layer near the contact point and obtain the correct Young’s angle θ_Y , we need to have $h_2 = \lambda^2 h_1$ with $\lambda = \frac{\pi \cos \theta_Y}{\pi - 2\theta_Y}$. We then derive the dynamic of the contact point which is consistent with the dynamic of the interface away from the contact point. We show that the improved threshold dynamics method still enjoys the energy-decaying property and is unconditionally stable. Furthermore, we also prove the Γ -convergence of the weighted functional (5) with $h_2 = \lambda^2 h_1$ to the functional (1). This extends the analysis in [13].

This paper is organized as follows. In Section 2, we derive the modified threshold dynamics method and prove that the modified method has energy-decaying property which implies the unconditional stability. In Section 3, we use asymptotic analysis to derive the dynamic law of the contact point. In Section 4, we prove the Γ -convergence result. We present several

numerical examples to verify the improvement of our modified method in Section 5. We then draw a conclusion and make some discussions in Section 6.

2. A modified threshold dynamics method for the wetting problem

In this section, we introduce a modified threshold dynamics method based on the recent work by Xu et al. [49]. The main idea in [49] is to extend the fluid domain Ω to a larger domain $\tilde{\Omega}$ (see Fig. 1) containing the solid phase. In the extended domain, the interface energies between different phases in (1) can be approximated by convolutions between characteristic functions and the Gaussian kernel $G_h(\mathbf{x})$ (see details below). In this paper, the interface energies between different phases are approximated by the convolutions between characteristic functions and Gaussian kernels with different h 's (e.g., h_1 for approximating liquid-vapor interface energy and h_2 for approximating solid-liquid and solid-vapor interface energy). Using the relaxation and linearization procedure introduced in [13], we derive a modified threshold dynamics method for wetting problems. From the consistency analysis, we derive the relationship between h_1 and h_2 so that the contact angle satisfies the Young's equation at the contact point both "microscopically" and "macroscopically". Here, we refer the local contact angle at the contact point as the microscopic angle and the apparent angle as the macroscopic angle. In general, microscopic angle is not necessarily equal to the apparent angle (see [7,36,49] and the references therein for more details).

2.1. Representation of interface energies in the extended domain

In the following, we let $D_1, D_2 \subset \Omega \subset \mathbb{R}^n$ be the liquid and vapor phases (see Fig. 1), respectively. Let $\Sigma_{LV} = \partial D_1 \cap \partial D_2$ be the liquid-vapor interface. When $h_1 \ll 1$, the area of Σ_{LV} can be approximated by (see [1,32])

$$|\Sigma_{LV}| \approx \frac{\sqrt{\pi}}{\sqrt{h_1}} \int \chi_{D_1} G_{h_1} * \chi_{D_2} \, \mathbf{d}\mathbf{x}, \tag{6}$$

where χ_{D_i} is the characteristic function of D_i and

$$G_{h_1}(\mathbf{x}) = \frac{1}{(4\pi h_1)^{n/2}} \exp\left(-\frac{|\mathbf{x}|^2}{4h_1}\right) \tag{7}$$

is the Gaussian kernel in \mathbb{R}^n . G_{h_2} and G_1 in the subsequent texts are similarly defined.

In the total energy (1), the second and third term are interface energies defined on the solid surface Γ . They are the solid-liquid interfacial energy term on $\Sigma_{SL} = \partial D_1 \cap \Gamma$ and the solid-vapor interfacial energy term on $\Sigma_{SV} = \partial D_2 \cap \Gamma$. To approximate these two terms using the Gaussian kernel, we extend the domain Ω beyond Γ (see Fig. 1). The extended domain is $\tilde{\Omega} = \Omega \cup D_3$ where D_3 is the solid region. Then, the solid surface is $\Gamma = \partial\Omega \cap \partial D_3$, the solid-liquid interface is $\Sigma_{SL} = \partial D_1 \cap \partial D_3$ and the solid-vapor interface is $\Sigma_{SV} = \partial D_2 \cap \partial D_3$.

From the observation and numerical experiments in [49], the apparent (macroscopic) angle always satisfies the Young's equation while the microscopic angle deviates from the correct Young's angle. There seems to be a boundary layer on the solid surface around the contact points. To modify the scheme, we use the convolutions between characteristic functions and the Gaussian kernel with a different parameter h_2 to approximate $|\Sigma_{SV}|$ and $|\Sigma_{SL}|$. That is,

$$|\Sigma_{SV}| \approx \frac{\sqrt{\pi}}{\sqrt{h_2}} \int \chi_{D_2} G_{h_2} * \chi_{D_3} \, \mathbf{d}\mathbf{x}, \tag{8}$$

$$|\Sigma_{SL}| \approx \frac{\sqrt{\pi}}{\sqrt{h_2}} \int \chi_{D_1} G_{h_2} * \chi_{D_3} \, \mathbf{d}\mathbf{x}. \tag{9}$$

Then, the total energy \mathcal{E} in (1) can be approximated by

$$\mathcal{E}^{h_1, h_2}(\chi_{D_1}, \chi_{D_2}) = \frac{\gamma_{LV}\sqrt{\pi}}{\sqrt{h_1}} \int_{\tilde{\Omega}} \chi_{D_1} G_{h_1} * \chi_{D_2} \, \mathbf{d}\mathbf{x} + \frac{\gamma_{SL}\sqrt{\pi}}{\sqrt{h_2}} \int_{\tilde{\Omega}} \chi_{D_1} G_{h_2} * \chi_{D_3} \, \mathbf{d}\mathbf{x} + \frac{\gamma_{SV}\sqrt{\pi}}{\sqrt{h_2}} \int_{\tilde{\Omega}} \chi_{D_2} G_{h_2} * \chi_{D_3} \, \mathbf{d}\mathbf{x}. \tag{10}$$

Denote $u_1 = \chi_{D_1}$ and $u_2 = \chi_{D_2}$. We define an admissible set:

$$\mathcal{B} = \{(u_1, u_2) \in BV(\Omega) \mid u_i(x) = 0, 1, \text{ and } u_1(x) + u_2(x) = 1, \text{ a.e. } x \in \Omega, \int_{\Omega} u_1 \, \mathbf{d}\mathbf{x} = V_0\}. \tag{11}$$

The wetting problem can be approximated by

$$\min_{(u_1, u_2) \in \mathcal{B}} \mathcal{E}^{h_1, h_2}(u_1, u_2). \tag{12}$$

This is a non-convex minimization problem since \mathcal{B} is not a convex set and the energy functional $\mathcal{E}^{h_1, h_2}(u_1, u_2)$ is concave.

2.2. Derivation of the modified threshold dynamics method

In this section, we present the derivation of a threshold dynamics method for the minimization problem (12). The derivation is based on the relaxation and linearization procedure introduced in [13]. Note that the problem (12) is to minimize a concave energy functional defined on a non-convex admissible set. However, we can relax this problem to an equivalent minimization problem in a convex admissible set. The relaxed problem is given by

$$\min_{(u_1, u_2) \in \mathcal{K}} \mathcal{E}^{h_1, h_2}(u_1, u_2) \tag{13}$$

where \mathcal{K} is the convex hull of the admissible set \mathcal{B} :

$$\mathcal{K} = \{(u_1, u_2) \in BV(\Omega) \mid 0 \leq u_i \leq 1, u_1(x) + u_2(x) = 1, \text{ a.e. } x \in \Omega, \int_{\Omega} u_1 \, d\mathbf{x} = V_0\}. \tag{14}$$

The following lemma shows that the relaxed problem (13) is equivalent to the original problem (12).

Lemma 2.1.

$$\min_{(u_1, u_2) \in \mathcal{K}} \mathcal{E}^{h_1, h_2}(u_1, u_2) = \min_{(u_1, u_2) \in \mathcal{B}} \mathcal{E}^{h_1, h_2}(u_1, u_2).$$

Proof. Let $(\tilde{u}_1, \tilde{u}_2) \in \mathcal{K}$ be a minimizer of the functional

$$\mathcal{E}^{h_1, h_2}(u_1, u_2).$$

Since $\mathcal{B} \subset \mathcal{K}$, we have

$$\begin{aligned} \mathcal{E}^{h_1, h_2}(\tilde{u}_1, \tilde{u}_2) &= \min_{(u_1, u_2) \in \mathcal{K}} \mathcal{E}^{h_1, h_2}(u_1, u_2) \\ &\leq \min_{(u_1, u_2) \in \mathcal{B}} \mathcal{E}^{h_1, h_2}(u_1, u_2). \end{aligned}$$

Therefore, we need only to prove that $(\tilde{u}_1, \tilde{u}_2) \in \mathcal{B}$.

We prove by contradiction. If $(\tilde{u}_1, \tilde{u}_2) \notin \mathcal{B}$, there is a set $A \in \Omega$ and a constant $0 < C_0 < \frac{1}{2}$, such that $|A| > 0$ and

$$0 < C_0 < \tilde{u}_1(x), \tilde{u}_2(x) < 1 - C_0, \text{ for all } x \in A.$$

We divide A into two sets $A = A_1 \cup A_2$ such that $A_1 \cap A_2 = \emptyset$ and $|A_1| = |A_2| = |A|/2$. Denote $u_1^t = \tilde{u}_1 + t\chi_{A_1} - t\chi_{A_2}$ and $u_2^t = \tilde{u}_2 - t\chi_{A_1} + t\chi_{A_2}$. When $0 < t < C_0$, we have $0 < u_1^t, u_2^t < 1$ and

$$u_1^t + u_2^t = \tilde{u}_1 + \tilde{u}_2 = 1, \text{ and } \int_{\Omega} u_1^t \, d\mathbf{x} = \int_{\Omega} \tilde{u}_1 \, d\mathbf{x} = V_0.$$

This implies that $(u_1^t, u_2^t) \in \mathcal{K}$. Furthermore, direct computations give,

$$\begin{aligned} \frac{d^2}{dt^2} \mathcal{E}^{h_1, h_2}(u_1^t, u_2^t) &= \frac{\sqrt{\pi}}{\sqrt{h_1}} \int_{\tilde{\Omega}} \frac{d}{dt} u_1^t G_{h_1} * \frac{d}{dt} u_2^t \, d\mathbf{x} \\ &= \frac{\sqrt{\pi}}{\sqrt{h_1}} \int_{\tilde{\Omega}} (\chi_{A_1} - \chi_{A_2}) G_{h_1} * (\chi_{A_2} - \chi_{A_1}) \, d\mathbf{x} \\ &= -\frac{\sqrt{\pi}}{\sqrt{h_1}} \int_{\tilde{\Omega}} (\chi_{A_1} - \chi_{A_2}) G_{h_1} * (\chi_{A_1} - \chi_{A_2}) \, d\mathbf{x} \\ &= -\frac{\sqrt{\pi}}{\sqrt{h_1}} \int_{\tilde{\Omega}} (G_{h_1/2} * (\chi_{A_1} - \chi_{A_2})) (G_{h_1/2} * (\chi_{A_1} - \chi_{A_2})) \, d\mathbf{x} \\ &\leq 0. \end{aligned}$$

The penultimate step comes from the fact that Gaussian kernel is a self-adjoint operator which is in a semi-group consisting of all Gaussian kernels with different values of h_1 . From above inequality, the functional is concave on the point $(\tilde{u}_1, \tilde{u}_2)$. Thus, $(\tilde{u}_1, \tilde{u}_2)$ cannot be a minimizer of the functional. This contradicts the assumption. \square

The above lemma implies that we can solve the relaxed problem (13) instead of the original one (12). In the following, we show that the relaxed problem can be solved iteratively using a threshold dynamics method.

Assume that in the k th iteration, we have the solution (u_1^k, u_2^k) , the energy functional $\mathcal{E}^{h_1, h_2}(u_1, u_2)$ can be linearized near the point (u_1^k, u_2^k) as follows:

$$\mathcal{E}^{h_1, h_2}(u_1, u_2) \approx \mathcal{E}^{h_1, h_2}(u_1^k, u_2^k) + \hat{\mathcal{L}}(u_1 - u_1^k, u_2 - u_2^k, u_1^k, u_2^k) + h.o.t.$$

with

$$\hat{\mathcal{L}}(u_1, u_2, u_1^k, u_2^k) = \sqrt{\pi} \left(\int_{\tilde{\Omega}} u_1 \left(\frac{\gamma_{LV}}{\sqrt{h_1}} G_{h_1} * u_2^k + \frac{\gamma_{SL}}{\sqrt{h_2}} G_{h_2} * \chi_{D_3} \right) dx + \int_{\tilde{\Omega}} u_2 \left(\frac{\gamma_{LV}}{\sqrt{h_1}} G_{h_1} * u_1^k + \frac{\gamma_{SV}}{\sqrt{h_2}} G_{h_2} * \chi_{D_3} \right) dx \right). \tag{15}$$

Note that, when u_1^k and u_2^k are given, the minimization of $\hat{\mathcal{L}}(u_1 - u_1^k, u_2 - u_2^k, u_1^k, u_2^k)$ is equivalent to the minimization of $\hat{\mathcal{L}}(u_1, u_2, u_1^k, u_2^k)$. Thus, instead of minimizing $\mathcal{E}^{h_1, h_2}(u_1, u_2)$, we minimize the linearized functional

$$\min_{(u_1, u_2) \in \mathcal{K}} \hat{\mathcal{L}}(u_1, u_2, u_1^k, u_2^k) \tag{16}$$

and set the solution to be (u_1^{k+1}, u_2^{k+1}) .

The following lemma shows that the minimization problem (16) is solved via a simple threshold dynamics method.

Lemma 2.2. Denote

$$\phi = \frac{1}{\sqrt{h_1}} G_{h_1} * (u_2^k - u_1^k) - \frac{\cos \theta_Y}{\sqrt{h_2}} G_{h_2} * \chi_{D_3}. \tag{17}$$

Let

$$D_1^{k+1} = \{x \in \Omega \mid \phi < \delta\} \tag{18}$$

for a proper δ such that $|D_1^{k+1}| = V_0$. Define $D_2^{k+1} = \Omega \setminus D_1^{k+1}$. Then $(u_1^{k+1}, u_2^{k+1}) = (\chi_{D_1^{k+1}}, \chi_{D_2^{k+1}})$ is the solution to (16).

Proof. Since $\hat{\mathcal{L}}$ is a linear functional, we need only to prove

$$\hat{\mathcal{L}}(u_1^{k+1}, u_2^{k+1}, u_1^k, u_2^k) \leq \hat{\mathcal{L}}(u_1, u_2, u_1^k, u_2^k), \tag{19}$$

for all $(u_1, u_2) \in \mathcal{B}$.

For each $(u_1, u_2) \in \mathcal{B}$, we know $u_1 = \chi_{\hat{D}_1}$ and $u_2 = \chi_{\hat{D}_2}$ for some open sets \hat{D}_1, \hat{D}_2 in Ω , such that $\hat{D}_1 \cap \hat{D}_2 = \emptyset$, $\hat{D}_1 \cup \hat{D}_2 = \Omega$ and $|\hat{D}_1| = V_0$. Let $A_1 = \hat{D}_1 \setminus D_1^{k+1} = D_2^{k+1} \setminus \hat{D}_2$ and $A_2 = \hat{D}_2 \setminus D_2^{k+1} = D_1^{k+1} \setminus \hat{D}_1$. We must have $|A_1| = |A_2|$ because of the volume conservation property. Since $A_1 \subset D_2^{k+1}$, we have

$$\phi(x) \geq \delta, \quad u_1^{k+1}(x) - u_1(x) = -1, \quad \forall x \in A_1.$$

Similarly, since $A_2 \subset D_1^{k+1}$, we have

$$\phi(x) < \delta, \quad u_1^{k+1}(x) - u_1(x) = 1, \quad \forall x \in A_2.$$

Therefore, using $u_1^{k+1} - u_1 + u_2^{k+1} - u_2 = 0$ and $\cos \theta_Y = \frac{\gamma_{SV} - \gamma_{SL}}{\gamma_{LV}}$, we have

$$\begin{aligned} & \hat{\mathcal{L}}(u_1^{k+1}, u_2^{k+1}, u_1^k, u_2^k) - \hat{\mathcal{L}}(u_1, u_2, u_1^k, u_2^k) \\ &= \sqrt{\pi} \int_{\tilde{\Omega}} (u_1^{k+1} - u_1) \left(\frac{\gamma_{LV}}{\sqrt{h_1}} G_{h_1} * u_2^k + \frac{\gamma_{SL}}{\sqrt{h_2}} G_{h_2} * \chi_{D_3} \right) + (u_2^{k+1} - u_2) \left(\frac{\gamma_{LV}}{\sqrt{h_1}} G_{h_1} * u_1^k + \frac{\gamma_{SV}}{\sqrt{h_2}} G_{h_2} * \chi_{D_3} \right) dx \\ &= \sqrt{\pi} \int_{\tilde{\Omega}} (u_1^{k+1} - u_1) \left(\frac{\gamma_{LV}}{\sqrt{h_1}} G_{h_1} * (u_2^k - u_1^k) + \frac{\gamma_{SL} - \gamma_{SV}}{\sqrt{h_2}} G_{h_2} * \chi_{D_3} \right) dx \end{aligned}$$

$$\begin{aligned}
 &= \sqrt{\pi} \gamma_{LV} \left(\int_{A_2} \phi \, d\mathbf{x} - \int_{A_1} \phi \, d\mathbf{x} \right) \\
 &\leq \delta \int_{A_2} d\mathbf{x} - \delta \int_{A_1} d\mathbf{x} = 0. \quad \square
 \end{aligned}$$

Now, we are led to the following threshold dynamics method:

Algorithm 1 A modified threshold dynamics method for solid wetting dynamics.

Given initial $D_1^0, D_2^0 \subset \Omega$ and solid domain D_3 , such that $D_1^0 \cap D_2^0 = \emptyset, D_1^0 \cup D_2^0 = \Omega$ and $|D_1^0| = V_0$. Set a tolerance parameter $\varepsilon > 0$, equilibrium angle θ_Y , time step h_1 , and time step h_2 .

1: For given sets (D_1^k, D_2^k) , calculate

$$\phi^k = \frac{1}{\sqrt{h_1}} G_{h_1} * (\chi_{D_2^k} - \chi_{D_1^k}) - \frac{\cos \theta_Y}{\sqrt{h_2}} G_{h_2} * \chi_{D_3}. \tag{20}$$

2: Find a δ such that the set

$$\tilde{D}_1^\delta = \{x \in \Omega \mid \phi < \delta\} \tag{21}$$

satisfies $|\tilde{D}_1^\delta| = V_0$. Denote $D_1^{k+1} = \tilde{D}_1^\delta$ and $D_2^{k+1} = \Omega \setminus D_1^{k+1}$.

3: If $|D_1^k - D_1^{k+1}| \leq \varepsilon$, stop; otherwise, go back to Step 1.

Remark 2.1.

1. The choice of h_1 and h_2 will be studied in the consistency analysis in Section 3.
2. The convolutions at the Step 1 can be efficiently computed using Fast Fourier transform (FFT).
3. At the Step 2, it is easy to check that $\phi(x)$ we defined is monotone across the liquid-vapor, solid-liquid, and solid-vapor interface. Denote $V(\delta) = |\tilde{D}_1^\delta|$, then $V(\delta)$ is strictly monotone with respect to δ when δ is around 0 and therefore the root of $V(\delta) - V_0$ exists uniquely. One may apply traditional iterative methods (e.g., the bisection method, the Newton’s method, the fixed point iteration, and so on) to find the unique root of $V(\delta) - V_0$ which is the value of δ preserving the volume of D_1 . However, the bisection method usually converges slow and the Newton’s method or the fixed point iteration is sensitive to the initial guesses. In [49], we proposed an efficient and stable algorithm to find the root of $V(\delta) - V_0$ based on the quick-sort algorithm.

2.3. Stability analysis

In this section, we will show that Algorithm 1 is stable, in the sense that the total energy of \mathcal{E}^{h_1, h_2} always decreases in the algorithm for any $h_1 > 0$ and $h_2 > 0$. We have the following theorem.

Theorem 2.1. Denote $(u_1^k, u_2^k) = (\chi_{D_1^k}, \chi_{D_2^k})$, $k = 0, 1, 2, \dots$, obtained in Algorithm 1. We have

$$\mathcal{E}^{h_1, h_2}(u_1^{k+1}, u_2^{k+1}) \leq \mathcal{E}^{h_1, h_2}(u_1^k, u_2^k), \tag{22}$$

for all $h_1 > 0$ and $h_2 > 0$.

Proof. By the definition of the linearization $\hat{\mathcal{L}}$ and Lemma 2.2, we know that

$$\begin{aligned}
 &\mathcal{E}^{h_1, h_2}(u_1^k, u_2^k) + \frac{\sqrt{\pi} \gamma_{LV}}{\sqrt{h_1}} \int_{\tilde{\Omega}} u_1^k G_{h_1} * u_2^k \, d\mathbf{x} = \hat{\mathcal{L}}(u_1^k, u_2^k, u_1^k, u_2^k) \\
 &\geq \mathcal{L}(u_1^{k+1}, u_2^{k+1}, u_1^k, u_2^k) = \mathcal{E}^{h_1, h_2}(u_1^{k+1}, u_2^{k+1}) \\
 &\quad + \frac{\sqrt{\pi} \gamma_{LV}}{\sqrt{h_1}} \left(\int_{\tilde{\Omega}} u_1^{k+1} G_{h_1} * u_2^k \, d\mathbf{x} + \int_{\tilde{\Omega}} u_2^{k+1} G_{h_1} * u_1^k \, d\mathbf{x} - \int_{\tilde{\Omega}} u_1^{k+1} G_{h_1} * u_2^{k+1} \, d\mathbf{x} \right).
 \end{aligned}$$

This leads to

$$\mathcal{E}^{h_1, h_2}(u_1^k, u_2^k) \geq \mathcal{E}^{h_1, h_2}(u_1^{k+1}, u_2^{k+1}) + I, \tag{23}$$

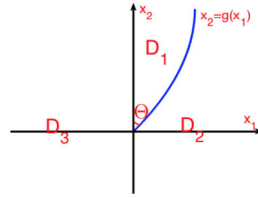


Fig. 2. Set up for the consistency analysis.

with

$$\begin{aligned}
 I &= \frac{\gamma_{LV} \sqrt{\pi}}{\sqrt{h_1}} \left(\int_{\tilde{\Omega}} u_1^{k+1} G_{h_1} * u_2^k \, d\mathbf{x} + \int_{\tilde{\Omega}} u_2^{k+1} G_{h_1} * u_1^k \, d\mathbf{x} - \int_{\tilde{\Omega}} u_1^{k+1} G_{h_1} * u_2^{k+1} \, d\mathbf{x} - \int_{\tilde{\Omega}} u_1^k G_{h_1} * u_2^k \, d\mathbf{x} \right) \\
 &= -\frac{\gamma_{LV} \sqrt{\pi}}{\sqrt{h_1}} \int_{\tilde{\Omega}} (u_1^{k+1} - u_1^k) G_{h_1} * (u_2^{k+1} - u_2^k) \, d\mathbf{x}.
 \end{aligned}$$

By the fact that $u_1^k + u_2^k = u_1^{k+1} + u_2^{k+1}$, we have

$$\begin{aligned}
 I &= \frac{\gamma_{LV} \sqrt{\pi}}{\sqrt{h_1}} \int_{\tilde{\Omega}} (u_1^{k+1} - u_1^k) G_{h_1} * (u_1^{k+1} - u_1^k) \, d\mathbf{x} \\
 &= \frac{\gamma_{LV} \sqrt{\pi}}{\sqrt{h_1}} \int_{\tilde{\Omega}} (G_{h_1/2} * (u_1^{k+1} - u_1^k)) (G_{h_1/2} * (u_1^{k+1} - u_1^k)) \, d\mathbf{x} \geq 0.
 \end{aligned}$$

Combining this inequality with (23) yields (22). □

3. Consistency analysis

In this section, we perform asymptotic analysis to determine h_1 and h_2 in Algorithm 1 with a very basic level of consistency with the correct contact angle at the contact point, in the sense that one step of Algorithm 1, acting on a set of liquid domain with smooth liquid-vapor interface and fixed solid surface (see Fig. 2). As for the dynamic of liquid-vapor interface away from the contact point, it is easy to check that our algorithm reduces the original two-phase volume preserving MBO method due to the exponentially decaying property of G_{h_2} (i.e., the effect from χ_{D_3} can be neglected when considering the behavior of the interface away from the solid surface). As for the behavior around the contact point, we perform the asymptotic analysis to derive the condition for the contact angle and the dynamic law of the contact point.

For simplicity, we focus on the 2-dimensional case. Without loss of generality, we assume the liquid-vapor interface is represented by $x_2 = g(x_1)$ ($x_1 \geq 0$) where $g(0) = 0$ and $g(x)$ is a smooth function defined on $[0, +\infty)$, the solid-liquid interface is represented by $x_1 = 0$ ($x_2 \geq 0$), and the solid-vapor interface is represented by $x_1 = 0$ ($x_2 < 0$). The main idea is to formally expand $\phi(\mathbf{x})$ and find the $\delta_{h_1,2}^{D_1,2}$ level set of the expanded $\phi(\mathbf{x})$ which is the updated interface at one time step according to Algorithm 1. Here, $\delta_{h_1,2}^{D_1,2}$ (depending on h_1, h_2, D_1 , and D_2) is the value for volume preserving at the Step 2 in Algorithm 1. Now, we first write

$$\begin{aligned}
 \phi(\mathbf{x}) &= \frac{1}{\sqrt{h_1}} G_{h_1} * (\chi_{D_2} - \chi_{D_1}) - \frac{\cos \theta_Y}{\sqrt{h_2}} G_{h_2} * \chi_{D_3} \\
 &= \frac{1}{\sqrt{h_1}} \left(\iint_{\mathbb{R}^2} G_{h_1}(\mathbf{x} - \mathbf{y}) (\chi_{D_2}(\mathbf{y}) - \chi_{D_1}(\mathbf{y})) \, d\mathbf{y} - \frac{\cos \theta_Y \sqrt{h_1}}{\sqrt{h_2}} \iint_{\mathbb{R}^2} G_{h_2}(\mathbf{x} - \mathbf{y}) \chi_{D_3}(\mathbf{y}) \, d\mathbf{y} \right) \\
 &= \frac{1}{\sqrt{h_1}} \left(\frac{1}{4\pi h_1} \iint_{D_2} \exp\left(-\frac{|\mathbf{x} - \mathbf{y}|^2}{4h_1}\right) \, d\mathbf{y} - \frac{1}{4\pi h_1} \iint_{D_1} \exp\left(-\frac{|\mathbf{x} - \mathbf{y}|^2}{4h_1}\right) \, d\mathbf{y} \right. \\
 &\quad \left. - \frac{\cos \theta_Y \sqrt{h_1}}{\sqrt{h_2}} \frac{1}{4\pi h_2} \iint_{D_3} \exp\left(-\frac{|\mathbf{x} - \mathbf{y}|^2}{4h_2}\right) \, d\mathbf{y} \right) \tag{24}
 \end{aligned}$$

$$\begin{aligned}
 &= \frac{1}{\sqrt{h_1}} \left(\frac{1}{4\pi h_1} \int_0^{+\infty} \int_{-\infty}^{+\infty} \exp\left(-\frac{(x_1 - y_1)^2 + (x_2 - y_2)^2}{4h_1}\right) dy_2 dy_1 \right. \\
 &\quad - \frac{1}{4\pi h_1} \int_0^{+\infty} \int_{g(y_1)}^{+\infty} \exp\left(-\frac{(x_1 - y_1)^2 + (x_2 - y_2)^2}{4h_1}\right) dy_2 dy_1 \\
 &\quad \left. - \frac{\cos \theta_Y \sqrt{h_1}}{\sqrt{h_2}} \frac{1}{4\pi h_2} \int_{-\infty}^0 \int_{-\infty}^{+\infty} \exp\left(-\frac{(x_1 - y_1)^2 + (x_2 - y_2)^2}{4h_2}\right) dy_2 dy_1 \right).
 \end{aligned}$$

Evaluating $\phi(\mathbf{x})$ at $x_1 = 0$ (i.e., the contact point only moves on the solid surface), we have

$$\phi(0, x_2) = \frac{1}{\sqrt{h_1}} (I_1 - I_2 - I_3) \tag{25}$$

where

$$\begin{aligned}
 I_1 &= \frac{1}{4\pi h_1} \int_0^{+\infty} \int_{-\infty}^{+\infty} \exp\left(-\frac{(y_1)^2 + (x_2 - y_2)^2}{4h_1}\right) dy_2 dy_1, \\
 I_2 &= \frac{1}{2\pi h_1} \int_0^{+\infty} \int_{g(y_1)}^{+\infty} \exp\left(-\frac{(y_1)^2 + (x_2 - y_2)^2}{4h_1}\right) dy_2 dy_1, \\
 I_3 &= \frac{\cos \theta_Y \sqrt{h_1}}{\sqrt{h_2}} \frac{1}{4\pi h_2} \int_{-\infty}^0 \int_{-\infty}^{+\infty} \exp\left(-\frac{(y_1)^2 + (x_2 - y_2)^2}{4h_2}\right) dy_2 dy_1.
 \end{aligned}$$

Direct calculation gives

$$I_1 = \frac{1}{2}, \tag{26}$$

$$I_3 = \frac{\cos \theta_Y \sqrt{h_1}}{2\sqrt{h_2}}. \tag{27}$$

Now, we only need to evaluate I_2 in the rest. For the convenience, we denote $\epsilon = \sqrt{h_1}$, $\tilde{y}_1 = \frac{y_1}{\epsilon}$, and $\tilde{y}_2 = \frac{y_2}{\epsilon}$. Also, we assume that $x_2 \sim O(\epsilon^2)$ (i.e., the motion of contact point is at the $O(h_1)$ time scale) and denote $\tilde{x}_2 = \frac{x_2}{\epsilon^2}$ which is the velocity of the contact point along the tangential direction of the solid surface. Then, we have

$$\begin{aligned}
 I_2 &= \frac{1}{2\pi} \int_0^{+\infty} \int_{\frac{g(\epsilon \tilde{y}_1)}{\epsilon}}^{+\infty} \exp\left(-\frac{\tilde{y}_1^2 + (\epsilon \tilde{x}_2 - \tilde{y}_2)^2}{4}\right) d\tilde{y}_2 d\tilde{y}_1 \\
 &= II_1 - II_2 - II_3
 \end{aligned} \tag{28}$$

where

$$\begin{aligned}
 II_1 &= \frac{1}{2\pi} \int_0^{+\infty} \int_0^{+\infty} \exp\left(-\frac{\tilde{y}_1^2 + (\epsilon \tilde{x}_2 - \tilde{y}_2)^2}{4}\right) d\tilde{y}_2 d\tilde{y}_1, \\
 II_2 &= \frac{1}{2\pi} \int_0^{+\infty} \int_0^{\tilde{y}_1 g'(\tilde{y}_1) + \epsilon \frac{\tilde{y}_1^2}{2} g''(\tilde{y}_1)} \exp\left(-\frac{\tilde{y}_1^2 + (\epsilon \tilde{x}_2 - \tilde{y}_2)^2}{4}\right) d\tilde{y}_2 d\tilde{y}_1, \\
 II_3 &= \frac{1}{2\pi} \int_0^{+\infty} \int_0^{\frac{g(\epsilon \tilde{y}_1)}{\epsilon}} \exp\left(-\frac{\tilde{y}_1^2 + (\epsilon \tilde{x}_2 - \tilde{y}_2)^2}{4}\right) d\tilde{y}_2 d\tilde{y}_1.
 \end{aligned}$$

Note that because of the exponentially decaying and smoothness of the Gaussian kernel, we have for a given ϵ , there exists an $M > 0$ with $M\epsilon = o(1)$ such that

$$\int_{|\mathbf{x}|>M} G_1(\mathbf{x})d\mathbf{x} = \exp\left(-\frac{M^2}{4}\right) = o(\epsilon). \tag{29}$$

Also, given a M , since $g(x)$ is smooth at $[0, +\infty)$, we have

$$\left| \frac{g(\epsilon \tilde{y}_1)}{\epsilon} - \tilde{y}_1 g'(0) - \epsilon \frac{\tilde{y}_1^2}{2} g''(0) \right| \leq C\epsilon^2 \tilde{y}_1^3 \tag{30}$$

for any $\tilde{y}_1 \in [0, M]$ and some constant $C > 0$. Here, for $\tilde{y}_1 \in [0, M]$, we have $\epsilon \tilde{y} = o(1)$ from $M\epsilon = o(1)$. Hence the constant C can be chosen as the maximum value of $g^{(3)}(\xi)$ for $\xi \in [0, 1]$ which is independent of M and ϵ .

Then, using (29) and (30), we have the following estimate on II_3 :

$$\begin{aligned} II_3 &= \frac{1}{2\pi} \int_0^M \int_{\tilde{y}_1 g'(0) + \epsilon \frac{\tilde{y}_1^2}{2} g''(0)}^{\frac{g(\epsilon \tilde{y}_1)}{\epsilon}} \exp\left(-\frac{\tilde{y}_1^2 + (\epsilon \tilde{x}_2 - \tilde{y}_2)^2}{4}\right) d\tilde{y}_2 d\tilde{y}_1 \\ &\quad + \frac{1}{2\pi} \int_M^{+\infty} \int_{\tilde{y}_1 g'(0) + \epsilon \frac{\tilde{y}_1^2}{2} g''(0)}^{\frac{g(\epsilon \tilde{y}_1)}{\epsilon}} \exp\left(-\frac{\tilde{y}_1^2 + (\epsilon \tilde{x}_2 - \tilde{y}_2)^2}{4}\right) d\tilde{y}_2 d\tilde{y}_1 \\ &= \frac{1}{2\pi} \int_0^M \int_{\tilde{y}_1 g'(0) + \epsilon \frac{\tilde{y}_1^2}{2} g''(0)}^{\frac{g(\epsilon \tilde{y}_1)}{\epsilon}} \exp\left(-\frac{\tilde{y}_1^2 + (\epsilon \tilde{x}_2 - \tilde{y}_2)^2}{4}\right) d\tilde{y}_2 d\tilde{y}_1 + o(\epsilon) \\ &\leq \frac{1}{2\pi} \int_0^M \int_{\tilde{y}_1 g'(0) + \epsilon \frac{\tilde{y}_1^2}{2} g''(0) - C\epsilon^2 \tilde{y}_1^3}^{\tilde{y}_1 g'(0) + \epsilon \frac{\tilde{y}_1^2}{2} g''(0) + C\epsilon^2 \tilde{y}_1^3} \exp\left(-\frac{\tilde{y}_1^2 + (\epsilon \tilde{x}_2 - \tilde{y}_2)^2}{4}\right) d\tilde{y}_2 d\tilde{y}_1 + o(\epsilon) \\ &= \frac{1}{2\pi} \int_0^M \exp\left(-\frac{\tilde{y}_1^2}{4}\right) \int_{\tilde{y}_1 g'(0) + \epsilon \frac{\tilde{y}_1^2}{2} g''(0) - C\epsilon^2 \tilde{y}_1^3}^{\tilde{y}_1 g'(0) + \epsilon \frac{\tilde{y}_1^2}{2} g''(0) + C\epsilon^2 \tilde{y}_1^3} \exp\left(-\frac{(\epsilon \tilde{x}_2 - \tilde{y}_2)^2}{4}\right) d\tilde{y}_2 d\tilde{y}_1 + o(\epsilon) \\ &\leq \frac{C\epsilon^2}{\pi} \int_0^M \tilde{y}_1^3 \exp\left(-\frac{\tilde{y}_1^2}{4}\right) d\tilde{y}_1 + o(\epsilon) \\ &= \frac{C\epsilon^2}{\pi} \left[\left(-2\tilde{y}_1^2 \exp\left(-\frac{\tilde{y}_1^2}{4}\right) \right) \Big|_0^M - \left(8 \exp\left(-\frac{\tilde{y}_1^2}{4}\right) \right) \Big|_0^M \right] + o(\epsilon) \\ &= \frac{C\epsilon^2}{\pi} \left[-2M^2 \exp\left(-\frac{M^2}{4}\right) - 8 \exp\left(-\frac{M^2}{4}\right) + 8 \right] + o(\epsilon) = o(\epsilon). \end{aligned} \tag{31}$$

For II_1 , we have

$$\begin{aligned} II_1 &= \frac{1}{2\pi} \int_{-\epsilon \tilde{x}_2}^{+\infty} \int_0^{+\infty} \exp\left(-\frac{\tilde{y}_1^2 + \tilde{y}_2'^2}{4}\right) d\tilde{y}_1 d\tilde{y}_2' \\ &= \frac{1}{2\pi} \int_0^{+\infty} \int_0^{+\infty} \exp\left(-\frac{\tilde{y}_1^2 + \tilde{y}_2'^2}{4}\right) d\tilde{y}_2' d\tilde{y}_1 + \frac{1}{2\pi} \int_{-\epsilon \tilde{x}_2}^0 \int_0^{+\infty} \exp\left(-\frac{\tilde{y}_1^2 + \tilde{y}_2'^2}{4}\right) d\tilde{y}_1 d\tilde{y}_2' \end{aligned} \tag{32}$$

$$\begin{aligned}
 &= \frac{1}{2} + \frac{1}{2\pi} \int_{-\epsilon\tilde{x}_2}^0 \int_0^{+\infty} \exp\left(-\frac{\tilde{y}'_1{}^2 + \tilde{y}'_2{}^2}{4}\right) d\tilde{y}'_1 d\tilde{y}'_2 \\
 &= \frac{1}{2} + \frac{1}{2\sqrt{\pi}} \int_{-\epsilon\tilde{x}_2}^0 \exp\left(-\frac{\tilde{y}'_2{}^2}{4}\right) d\tilde{y}'_2 \\
 &= \frac{1}{2} + \frac{1}{2\sqrt{\pi}} \int_{-\epsilon\tilde{x}_2}^0 \left(1 - \frac{\tilde{y}'_2{}^2}{4} + \frac{\tilde{y}'_2{}^4}{4^2 2!} - \frac{\tilde{y}'_2{}^6}{4^3 3!} + \dots\right) d\tilde{y}'_2 = \frac{1}{2} + \frac{\epsilon\tilde{x}_2}{2\sqrt{\pi}} + o(\epsilon).
 \end{aligned}$$

For II_2 , using (29) to make the integrating range of \tilde{y}_1 belong to the radius of convergence of the expansion of $G_1(\mathbf{x})$, we then have

$$\begin{aligned}
 II_2 &= \frac{1}{2\pi} \int_0^M \int_0^{\tilde{y}_1 g'(0) + \epsilon \frac{\tilde{y}_1^2}{2} g''(0)} \exp\left(-\frac{\tilde{y}_1^2 + (\epsilon\tilde{x}_2 - \tilde{y}_2)^2}{4}\right) d\tilde{y}_2 d\tilde{y}_1 + o(\epsilon) \\
 &= \frac{1}{2\pi} \int_0^M \int_{-\epsilon\tilde{x}_2}^{\tilde{y}_1 g'(0) + \epsilon \frac{\tilde{y}_1^2}{2} g''(0) - \epsilon\tilde{x}_2} \exp\left(-\frac{\tilde{y}_1^2 + \tilde{y}_2'^2}{4}\right) d\tilde{y}_2' d\tilde{y}_1 + o(\epsilon) \\
 &= \frac{1}{2\pi} \int_0^M \exp\left(-\frac{\tilde{y}_1^2}{4}\right) (III_1 + III_2 + III_3) d\tilde{y}_1 + o(\epsilon)
 \end{aligned} \tag{33}$$

where

$$\begin{aligned}
 III_1 &= \int_{-\epsilon\tilde{x}_2}^0 \exp\left(-\frac{\tilde{y}_2'^2}{4}\right) d\tilde{y}_2', \\
 III_2 &= \int_0^{\tilde{y}_1 g'(0)} \exp\left(-\frac{\tilde{y}_2'^2}{4}\right) d\tilde{y}_2', \\
 III_3 &= \int_{\tilde{y}_1 g'(0)}^{\tilde{y}_1 g'(0) + \epsilon \frac{\tilde{y}_1^2}{2} g''(0) - \epsilon\tilde{x}_2} \exp\left(-\frac{\tilde{y}_2'^2}{4}\right) d\tilde{y}_2'.
 \end{aligned}$$

For III_1 , we have

$$III_1 = \int_{-\epsilon\tilde{x}_2}^0 \left(1 - \frac{\tilde{y}_2'^2}{4} + \frac{\tilde{y}_2'^4}{4^2 2!} - \frac{\tilde{y}_2'^6}{4^3 3!} + \dots\right) d\tilde{y}_2' = \epsilon\tilde{x}_2 + o(\epsilon).$$

Then,

$$\frac{1}{2\pi} \int_0^M \exp\left(-\frac{\tilde{y}_1^2}{4}\right) III_1 d\tilde{y}_1 = \frac{\epsilon\tilde{x}_2}{2\sqrt{\pi}} + o(\epsilon). \tag{34}$$

Similarly, for III_3 , we have

$$III_3 = \int_{\tilde{y}_1 g'(0)}^{\tilde{y}_1 g'(0) + \epsilon \frac{\tilde{y}_1^2}{2} g''(0) - \epsilon\tilde{x}_2} \left(1 - \frac{\tilde{y}_2'^2}{4} + \frac{\tilde{y}_2'^4}{4^2 2!} - \frac{\tilde{y}_2'^6}{4^3 3!} + \dots\right) d\tilde{y}_2'$$

$$\begin{aligned}
 &= \epsilon \left(\frac{\tilde{y}_1^2}{2} g''(0) - \tilde{x}_2 - \frac{(\frac{\tilde{y}_1^2}{2} g''(0) - \tilde{x}_2)(\tilde{y}_1 g'(0))^2}{4} + \frac{(\frac{\tilde{y}_1^2}{2} g''(0) - \tilde{x}_2)(\tilde{y}_1 g'(0))^4}{4^2 2!} - \dots \right) + o(\epsilon) \\
 &= \epsilon \left(\frac{\tilde{y}_1^2}{2} g''(0) - \tilde{x}_2 \right) \exp\left(-\frac{(\tilde{y}_1 g'(0))^2}{4}\right) + o(\epsilon).
 \end{aligned}$$

Then,

$$\begin{aligned}
 \frac{1}{2\pi} \int_0^M \exp\left(-\frac{\tilde{y}_1^2}{4}\right) III_3 d\tilde{y}_1 &= \frac{\epsilon}{2\pi} \int_0^{+\infty} \left(\exp\left(-\frac{\tilde{y}_1^2(1+(g'(0))^2)}{4}\right) \right) \left(\frac{\tilde{y}_1^2}{2} g''(0) - \tilde{x}_2 \right) d\tilde{y}_1 + o(\epsilon) \\
 &= \frac{\epsilon}{2\sqrt{\pi}\sqrt{1+(g'(0))^2}} \left(\frac{g''(0)}{1+(g'(0))^2} - \tilde{x}_2 \right) + o(\epsilon).
 \end{aligned} \tag{35}$$

For III_2 , we have

$$\begin{aligned}
 \frac{1}{2\pi} \int_0^M \exp\left(-\frac{\tilde{y}_1^2}{4}\right) III_2 d\tilde{y}_1 &= \frac{1}{2\pi} \int_0^{+\infty} \exp\left(-\frac{\tilde{y}_1^2}{4}\right) \int_0^{\tilde{y}_1 g'(0)} \exp\left(-\frac{\tilde{y}_2^2}{4}\right) d\tilde{y}_2 d\tilde{y}_1 + o(\epsilon) \\
 &= \frac{1}{2\pi} \int_0^{\frac{\pi}{2}-\Theta} \int_0^{+\infty} \exp\left(-\frac{r^2}{4}\right) r dr d\theta + o(\epsilon) \\
 &= \frac{\frac{\pi}{2}-\Theta}{\pi} + o(\epsilon)
 \end{aligned} \tag{36}$$

where $\Theta = \pi/2 - \arctan(g'(0))$ (see Fig. 2).

Combining (34), (35), and (36) yields:

$$\begin{aligned}
 II_2 &= \frac{\epsilon \tilde{x}_2}{2\sqrt{\pi}} + \frac{\epsilon}{2\sqrt{\pi}\sqrt{1+(g'(0))^2}} \left(\frac{g''(0)}{1+(g'(0))^2} - \tilde{x}_2 \right) + \frac{\frac{\pi}{2}-\Theta}{\pi} + o(\epsilon) \\
 &= \frac{\frac{\pi}{2}-\Theta}{\pi} + \frac{\epsilon}{2\sqrt{\pi}} \left(\left(1 - \frac{1}{\sqrt{1+(g'(0))^2}} \right) \tilde{x}_2 + \frac{g''(0)}{(1+(g'(0))^2)^{\frac{3}{2}}} \right) + o(\epsilon).
 \end{aligned} \tag{37}$$

Combining (31), (32), and (37) yields:

$$\begin{aligned}
 I_2 &= \frac{1}{2} + \frac{\epsilon \tilde{x}_2}{2\sqrt{\pi}} - \frac{\frac{\pi}{2}-\Theta}{\pi} - \frac{\epsilon}{2\sqrt{\pi}} \left(\left(1 - \frac{1}{\sqrt{1+(g'(0))^2}} \right) \tilde{x}_2 + \frac{g''(0)}{(1+(g'(0))^2)^{\frac{3}{2}}} \right) + o(\epsilon) \\
 &= \frac{1}{2} - \frac{\frac{\pi}{2}-\Theta}{\pi} + \frac{\epsilon}{2\sqrt{\pi}} \left(\frac{\tilde{x}_2}{\sqrt{1+(g'(0))^2}} - \frac{g''(0)}{(1+(g'(0))^2)^{\frac{3}{2}}} \right) + o(\epsilon).
 \end{aligned} \tag{38}$$

Combining (26), (27), and (38) yields:

$$\phi(0, x_2) = \frac{1}{\epsilon} \left(\frac{\frac{\pi}{2}-\Theta}{\pi} - \frac{\cos\theta_Y \sqrt{h_1}}{2\sqrt{h_2}} - \frac{\epsilon}{2\sqrt{\pi}} \left(\frac{\tilde{x}_2}{\sqrt{1+(g'(0))^2}} - \frac{g''(0)}{(1+(g'(0))^2)^{\frac{3}{2}}} \right) + o(\epsilon) \right). \tag{39}$$

Let

$$\phi(0, x_2) = \delta_{h_{1,2}}^{D_{1,2}} \tag{40}$$

with $\delta_{h_{1,2}}^{D_{1,2}} \sim O(1)$, collecting all the terms at the order of $O(\frac{1}{\epsilon})$ in (40), we have:

$$\frac{\frac{\pi}{2}-\Theta}{\pi} = \frac{\cos\theta_Y \sqrt{h_1}}{2\sqrt{h_2}} \tag{41}$$

which is

$$\Theta = \frac{\pi}{2} \left(1 - \frac{\cos\theta_Y \sqrt{h_1}}{\sqrt{h_2}} \right). \tag{42}$$

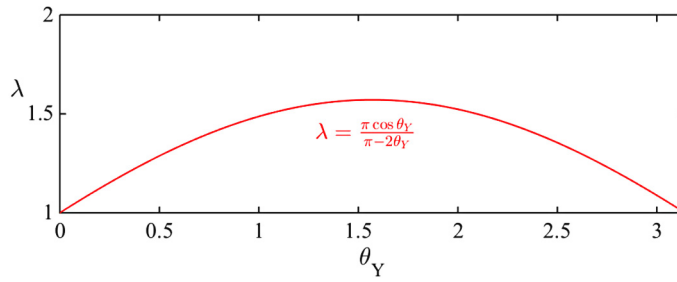


Fig. 3. Relationship between λ and θ_Y where $\lambda = \frac{\sqrt{h_2}}{\sqrt{h_1}}$.

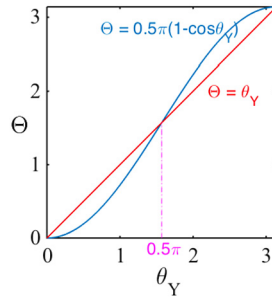


Fig. 4. Relationship between Θ and θ_Y when $h_1 = h_2$.

Define

$$\lambda(\theta_Y) = \frac{\sqrt{h_2}}{\sqrt{h_1}} = \frac{\pi \cos \theta_Y}{\pi - 2\theta_Y}, \quad \theta_Y \in [0, \pi] \tag{43}$$

with $\lambda(\frac{\pi}{2}) = \frac{\pi}{2}$ (see Fig. 3) and therefore we have

$$h_2 = \left(\frac{\pi \cos \theta_Y}{\pi - 2\theta_Y} \right)^2 h_1. \tag{44}$$

Submitting (44) into (42) gives us $\Theta = \theta_Y$ for any $\theta_Y \in [0, \pi]$.

Remark 3.1. We remark here that from (42), we get that the angle condition is independent of the initial condition and thus implying that there is no relaxation dynamics of the contact angle in this specific model. To keep the consistency of the scheme, we impose $\Theta = \theta_Y$ to get the relation between h_1 and h_2 . One can also interpret that this model is in the regime where the relaxation dynamics of the contact angle is at a very fast time scale.

Note that, when $h_1 = h_2$, Algorithm 1 reduces to the original threshold dynamics method proposed in [49]. Then, the contact angle Θ satisfies

$$\Theta = \frac{\pi}{2} (1 - \cos \theta_Y) \tag{45}$$

as plotted in Fig. 4. It is consistent with the observation and numerical experiments in [49].

Collecting all the terms at the order of $O(1)$ in (40) yields:

$$\frac{\tilde{x}_2}{\sqrt{1 + (g'(0))^2}} - \frac{g''(0)}{(1 + (g'(0))^2)^{\frac{3}{2}}} = -2\sqrt{\pi} \delta_{h_{1,2}}^{D_{1,2}}. \tag{46}$$

Then, we further have

$$\tilde{x}_2 = \sqrt{1 + (g'(0))^2} \left(\frac{g''(0)}{(1 + (g'(0))^2)^{\frac{3}{2}}} - 2\sqrt{\pi} \delta_{h_{1,2}}^{D_{1,2}} \right). \tag{47}$$

From the definition of $g(x_1)$ and Θ , fundamental calculations give that $\sqrt{1 + (g'(0))^2} = \sqrt{1 + \cot(\Theta)^2} = \frac{1}{\sin \Theta}$ and $\kappa = \frac{g''(0)}{(1 + (g'(0))^2)^{\frac{3}{2}}}$ where κ is the mean curvature defined at $(0, 0)$ by the limit along the liquid-vapor interface. Then, we have:

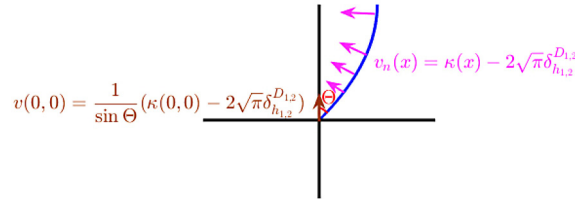


Fig. 5. The diagram for the motion law at the contact point and liquid-vapor interface away from the solid surface.

$$\tilde{x}_2 = \frac{1}{\sin \Theta} \left(\kappa - 2\sqrt{\pi} \delta_{h_{1,2}}^{D_{1,2}} \right), \tag{48}$$

where $2\sqrt{\pi} \delta_{h_{1,2}}^{D_{1,2}}$ is a parameter dependent on D_1, D_2, h_1 and h_2 for the volume preserving. Formally, $2\sqrt{\pi} \delta_{h_{1,2}}^{D_{1,2}} = \bar{\kappa}$ where $\bar{\kappa}$ is the average of κ along the liquid-vapor interface. Since \tilde{x}_2 is the velocity of the contact point moving along the solid surface which is consistent with the motion law at the interface away from the solid surface (see Fig. 5 and see [26] for more details on the derivation of the motion law for the two-phase interface with no contact points).

4. Gamma-Convergence of the weighted functional

In this section, we will study the Γ -convergence of the weighted functional \mathcal{E}^{h_1, h_2} with $h_2 = \lambda^2 h_1$ to the total surface energy \mathcal{E} for any given λ . For clarity, we first introduce some notations. Denote the functional space

$$\mathbb{X} := \{u \in BV(\tilde{\Omega}) : u = \chi_{\Omega_1}, \Omega_1 \subset \Omega, |\Omega_1| = V_0\}. \tag{49}$$

In \mathbb{X} , the norm of a function u is defined as

$$\|u\|_{BV} = \|u\|_{L^1(\tilde{\Omega})} + \int_{\tilde{\Omega}} |Du|.$$

By definition,

$$\int_{\tilde{\Omega}} |Du| = \sup_{\phi} \left\{ \int_{\tilde{\Omega}} u \operatorname{div} \phi dx : \phi \in C_c^1(\tilde{\Omega}, \mathbb{R}^n) \right\}.$$

We also rewrite the modified energy functional $\mathcal{E}^{h_1, h_2}(\Omega_1, \Omega_2)$ with $h_2 = \lambda^2 h_1$ as a functional on $u = \chi_{\Omega_1} \in \mathbb{X}$,

$$\tilde{\mathcal{E}}_h(u) = \frac{\sqrt{\pi} \gamma_{LV}}{\sqrt{h}} \int_{\tilde{\Omega}} u G_h * (\chi_{\Omega} - u) dx + \frac{\sqrt{\pi} \gamma_{SL}}{\sqrt{\lambda^2 h}} \int_{\tilde{\Omega}} u G_{\lambda^2 h} * \chi_{\Omega_3} dx + \frac{\sqrt{\pi} \gamma_{SV}}{\sqrt{\lambda^2 h}} \int_{\tilde{\Omega}} (\chi_{\Omega} - u) G_{\lambda^2 h} * \chi_{\Omega_3} dx.$$

Using the Young's equation $\gamma_{SV} - \gamma_{SL} = \gamma_{LV} \cos \theta_Y$, a simple computation leads to

$$\tilde{\mathcal{E}}_h(u) = \frac{\sqrt{\pi} \gamma_{LV}}{\sqrt{h}} \int_{\tilde{\Omega}} u G_h * (\chi_{\Omega} - u) dx - \frac{\sqrt{\pi} \gamma_{LV} \cos \theta_Y}{\sqrt{\lambda^2 h}} \int_{\tilde{\Omega}} u G_{\lambda^2 h} * \chi_{\Omega_3} dx + \frac{\sqrt{\pi} \gamma_{SV}}{\sqrt{\lambda^2 h}} \int_{\tilde{\Omega}} \chi_{\Omega} G_{\lambda^2 h} * \chi_{\Omega_3} dx. \tag{50}$$

Similarly, the functional (3) without rescaling reduces to

$$\mathcal{E}_h(u) = \frac{\sqrt{\pi} \gamma_{LV}}{\sqrt{h}} \int_{\tilde{\Omega}} u G_h * (\chi_{\Omega} - u) dx - \frac{\sqrt{\pi} \gamma_{LV} \cos \theta_Y}{\sqrt{h}} \int_{\tilde{\Omega}} u G_h * \chi_{\Omega_3} dx + \frac{\sqrt{\pi} \gamma_{SV}}{\sqrt{h}} \int_{\tilde{\Omega}} \chi_{\Omega} G_h * \chi_{\Omega_3} dx. \tag{51}$$

We note the energy functional \mathcal{E} can be rewritten as

$$\begin{aligned} \mathcal{E}(u) &= \gamma_{LV} |\Sigma_{LV}| - \gamma_{LV} \cos \theta_Y |\Sigma_{SL}| + \gamma_{SV} |\Gamma| \\ &= \gamma_{LV} \int_{\tilde{\Omega}} (|Du| + |D(\chi_{\Omega} - u)| - |D\chi_{\Omega}|) - \gamma_{LV} \cos \theta_Y \int_{\tilde{\Omega}} (|Du| + |D(\chi_{\Omega_3})| - |D(u + \chi_{\Omega_3})|) + \gamma_{SV} |\Gamma| \end{aligned} \tag{52}$$

where Γ is the interface between Ω and Ω_3 .

We first state a result on the convergence of \mathcal{E}_h to \mathcal{E} , as given in the following proposition.

Proposition 4.1. *The functional \mathcal{E}_h Γ -converges to \mathcal{E} in \mathbb{X} as h goes to zero.*

The proof of the proposition is essentially given in [13], where the Γ -convergence is proved for a multi-phase problem. Here we will not repeat the details of the proof and refer to the Appendix in [13].

We aim to show the Γ -convergence of $\tilde{\mathcal{E}}_h$ to \mathcal{E} . It turns out the result can not be proved directly by the method in [13]. In the following we will use an indirect method to prove the result. We introduce a few more notations. Denote

$$\mathcal{F}_h(u) = -\frac{\sqrt{\pi}\gamma_{LV}\cos\theta_Y}{\sqrt{h}} \int_{\tilde{\Omega}} uG_h * \chi_{\Omega_3} dx + \frac{\sqrt{\pi}\gamma_{SV}}{\sqrt{h}} \int_{\tilde{\Omega}} \chi_{\Omega} G_h * \chi_{\Omega_3} dx, \tag{53}$$

and

$$\mathcal{F}(u) = -\gamma_{LV}\cos\theta_Y \int_{\tilde{\Omega}} (|Du| + |D(\chi_{\Omega_3})| - |D(u + \chi_{\Omega_3})|) + \gamma_{SV}|\Sigma|. \tag{54}$$

We will prove the following proposition.

Proposition 4.2. *The functional \mathcal{F}_h converges to \mathcal{F} continuously in \mathbb{X} as h goes to zero.*

We recall the definition of continuous convergence in [27]. A series of functional \mathcal{F}_h converge to \mathcal{F} continuously in \mathbb{X} , if for given $u \in \mathbb{X}$ and for any small positive number ε , there exists a $h_0 > 0$ and a neighborhood $\mathcal{N}(u)$ of u such that

$$|\mathcal{F}_h(v) - \mathcal{F}(u)| < \varepsilon, \quad \forall v \in \mathcal{N}(u). \tag{55}$$

To prove Proposition 4.2, we need a few more preparations. We will prove two simple lemmas.

Lemma 4.1. *For any $\chi_{\hat{\Omega}_1}, \chi_{\hat{\Omega}_2} \in \mathbb{X}$, if $\hat{\Omega}_1 \cap \hat{\Omega}_2 = \emptyset$, we have*

$$\int_{\tilde{\Omega}} |D(\chi_{\hat{\Omega}_1} - \chi_{\hat{\Omega}_2})| = \int_{\tilde{\Omega}} |D(\chi_{\hat{\Omega}_1})| + \int_{\tilde{\Omega}} |D(\chi_{\hat{\Omega}_2})|.$$

Proof. Since $\hat{\Omega}_1 \cap \hat{\Omega}_2 = \emptyset$, for any $\phi \in C_c^1(\tilde{\Omega})$, we have

$$\int_{\tilde{\Omega}} (\chi_{\hat{\Omega}_1} - \chi_{\hat{\Omega}_2}) \operatorname{div} \phi dx = \int_{\tilde{\Omega}_1} \operatorname{div} \phi dx - \int_{\tilde{\Omega}_2} \operatorname{div} \phi dx = \int_{\partial^* \hat{\Omega}_1} \phi \cdot \mathbf{n}_1 d\mathcal{H}^{n-1}(x) - \int_{\partial^* \hat{\Omega}_2} \phi \cdot \mathbf{n}_2 d\mathcal{H}^{n-1}(x),$$

where $\partial^* \hat{\Omega}_i$ is the reduced boundary of $\hat{\Omega}_i$ and \mathbf{n}_i are the outer normal of corresponding domain $\hat{\Omega}_i$, $i = 1, 2$. Suppose $\partial^* \hat{\Omega}_1 \cap \partial^* \hat{\Omega}_2 = \hat{\Gamma}$, then we have $\mathbf{n}_1 = -\mathbf{n}_2$ on $\hat{\Gamma}$. Suppose we can choose a $\phi \in C_c^1(\tilde{\Omega})$ such that $\phi = \mathbf{n}_1$ on $\partial^* \hat{\Omega}_1$ and $-\mathbf{n}_2$ on $\partial^* \hat{\Omega}_2 \setminus \hat{\Gamma}$. When the boundary $\partial^* \hat{\Omega}_i$ are smooth, such a ϕ always exists in $C_c^1(\tilde{\Omega})$. Otherwise, we can choose a series of functions in $C_c^1(\tilde{\Omega})$ to approximate ϕ . For such a choice of ϕ , we have

$$\int_{\tilde{\Omega}} (\chi_{\hat{\Omega}_1} - \chi_{\hat{\Omega}_2}) \operatorname{div} \phi dx = |\partial^* \hat{\Omega}_1| + |\partial^* \hat{\Omega}_2|$$

Using the basic relation $\int_{\tilde{\Omega}} |D\chi_{\hat{\Omega}_i}| = |\partial^* \hat{\Omega}_i|$, the above equation reads

$$\int_{\tilde{\Omega}} (\chi_{\hat{\Omega}_1} - \chi_{\hat{\Omega}_2}) \operatorname{div} \phi dx = \int_{\tilde{\Omega}} |D\chi_{\hat{\Omega}_1}| + \int_{\tilde{\Omega}} |D\chi_{\hat{\Omega}_2}|.$$

By the definition, we deduce

$$\int_{\tilde{\Omega}} |D(\chi_{\hat{\Omega}_1} - \chi_{\hat{\Omega}_2})| \geq \int_{\tilde{\Omega}} |D\chi_{\hat{\Omega}_1}| + \int_{\tilde{\Omega}} |D\chi_{\hat{\Omega}_2}|.$$

Together with the triangle inequality,

$$\int_{\tilde{\Omega}} |D(\chi_{\hat{\Omega}_1} - \chi_{\hat{\Omega}_2})| \leq \int_{\tilde{\Omega}} |D\chi_{\hat{\Omega}_1}| + \int_{\tilde{\Omega}} |D\chi_{\hat{\Omega}_2}|,$$

we have proved the lemma. \square

The statement in the next lemma is already given in [13]. Here we state it clearly for convenience of readers.

Lemma 4.2. For any $\chi_{\hat{\Omega}} \in \mathbb{X}$, we have

$$\left| \frac{\sqrt{\pi}}{\sqrt{h}} \int_{\hat{\Omega}} \chi_{\hat{\Omega}} G_h * \chi_{\hat{\Omega}^c} dx \right| \leq \int_{\hat{\Omega}} |D(\chi_{\hat{\Omega}_1})|,$$

where $\hat{\Omega}^c = \tilde{\Omega} \setminus \hat{\Omega}$ and c_0 is a constant independent of the choice of $\hat{\Omega}$.

Proof. Use the definition of the Gaussian kernel. A direct computation shows that

$$\begin{aligned} \frac{\sqrt{\pi}}{\sqrt{h}} \int_{\hat{\Omega}} \chi_{\hat{\Omega}} G_h * \chi_{\hat{\Omega}^c} dx &= \frac{\sqrt{\pi}}{\sqrt{h}} \int_{\hat{\Omega}} \chi_{\hat{\Omega}}(x) \int_{\mathbb{R}^n} G_h(y-x) \chi_{\hat{\Omega}^c}(y) dy dx \\ &= \frac{\sqrt{\pi}}{\sqrt{h}} \int_{\hat{\Omega}} \chi_{\hat{\Omega}}(x) \int_{\mathbb{R}^n} G_h(\xi) \chi_{\hat{\Omega}^c}(x+\xi) d\xi dx \\ &= \frac{\sqrt{\pi}}{\sqrt{h}} \int_{\hat{\Omega}} \chi_{\hat{\Omega}}(x) \int_{\mathbb{R}^n} G_1(\xi) \chi_{\hat{\Omega}^c}(x+\sqrt{h}\xi) d\xi dx \\ &= \frac{\sqrt{\pi}}{\sqrt{h}} \int_{\mathbb{R}^n} G_1(\xi) \int_{\hat{\Omega}} \chi_{\hat{\Omega}}(x) \chi_{\hat{\Omega}^c}(x+\sqrt{h}\xi) dx d\xi \\ &= \sqrt{\pi} \int_0^\infty r^n G(r) \frac{1}{r\sqrt{h}} \int_{S^{n-1}} \int_{\hat{\Omega}} \chi_{\hat{\Omega}}(x) \chi_{\hat{\Omega}^c}(x+\sqrt{h}\xi) dx dS dr \\ &\leq \sqrt{\pi} \int_0^\infty r^n G(r) dr \sup_r \left| \frac{1}{r\sqrt{h}} \int_{S^{n-1}} \int_{\hat{\Omega}} \chi_{\hat{\Omega}}(x) (\chi_{\hat{\Omega}^c}(x+\sqrt{h}\xi) - \chi_{\hat{\Omega}^c}(x)) dx dS \right| \end{aligned}$$

Further calculation gives

$$\begin{aligned} &\left| \frac{1}{r\sqrt{h}} \int_{S^{n-1}} \int_{\hat{\Omega}} \chi_{\hat{\Omega}}(x) (\chi_{\hat{\Omega}^c}(x+\sqrt{h}\xi) - \chi_{\hat{\Omega}^c}(x)) dx dS \right| \\ &\leq \left| \frac{1}{r\sqrt{h}} \int_{S^{n-1}} \int_{\hat{\Omega}} |(\chi_{\hat{\Omega}^c}(x+\sqrt{h}\xi) - \chi_{\hat{\Omega}^c}(x))| dx dS \right| \\ &\leq |S^{n-1}| \int_{\hat{\Omega}} |D\chi_{\hat{\Omega}}|. \end{aligned}$$

Notice that $|S^{n-1}| \int_0^\infty r^n G(r) dr = \sqrt{\pi}$, we have proved the lemma. \square

Proof of Proposition 4.2. We will prove the proposition by definition. Firstly, it is known that (see [1,32])

$$\lim_{h \rightarrow 0} \frac{\sqrt{\pi} \gamma_{SV}}{\sqrt{h}} \int_{\hat{\Omega}} \chi_{\Omega} G_h * \chi_{\Omega_3} dx = \gamma_{SV} |\Sigma|.$$

Therefore, for any ε , there exists a constant h_0 such that for any $h < h_0$,

$$\left| \frac{\sqrt{\pi} \gamma_{SV}}{\sqrt{h}} \int_{\hat{\Omega}} \chi_{\Omega} G_h * \chi_{\Omega_3} dx - \gamma_{SV} |\Sigma| \right| \leq \frac{\varepsilon}{4}. \tag{56}$$

Similarly, for any given $u \in \mathbb{X}$ and for any ε , there exists a $h_1 > 0$, such that for any $h < h_1$,

$$\left| -\frac{\sqrt{\pi} \gamma_{LV} \cos \theta_Y}{\sqrt{\lambda^2 h}} \int_{\hat{\Omega}} u G_h * \chi_{\Omega_3} dx + \gamma_{LV} \cos \theta_Y \int_{\hat{\Omega}} (|Du| + |D(\chi_{\Omega_3})| - |D(u + \chi_{\Omega_3})|) \right| \leq \frac{\varepsilon}{4}. \tag{57}$$

Combine them together, we have

$$|\mathcal{F}_h(u) - \mathcal{F}(u)| \leq \frac{\varepsilon}{2}, \tag{58}$$

for all $h < h^* = \min(h_0, h_1)$.

Denote $u = \chi_{\Omega_1}$. For any $v \in \mathbb{X}$, we know that $v = \chi_{\hat{\Omega}_1}$ for some $\hat{\Omega}_1 \subset \Omega$. Then $u - v = \chi_{\Omega_1} - \chi_{\hat{\Omega}_1} = \chi_{\Omega_1 \setminus \hat{\Omega}_1} - \chi_{\hat{\Omega}_1 \setminus \Omega_1}$, with $(\Omega_1 \setminus \hat{\Omega}_1) \cap (\hat{\Omega}_1 \setminus \Omega_1) = \emptyset$. Then we have

$$\begin{aligned} |\mathcal{F}_h(u) - \mathcal{F}_h(v)| &= \frac{\sqrt{\pi} \gamma_{LV} |\cos \theta_Y|}{\sqrt{h}} \left| \int_{\tilde{\Omega}} (u - v) G_h * \chi_{\Omega_3} dx \right| \\ &= \frac{\sqrt{\pi} \gamma_{LV} |\cos \theta_Y|}{\sqrt{h}} \left| \int_{\Omega_1 \setminus \hat{\Omega}_1} G_h * \chi_{\Omega_3} dx - \int_{\hat{\Omega}_1 \setminus \Omega_1} G_h * \chi_{\Omega_3} dx \right| \\ &\leq \frac{\sqrt{\pi} \gamma_{LV} |\cos \theta_Y|}{\sqrt{h}} \left(\int_{\Omega_1 \setminus \hat{\Omega}_1} G_h * \chi_{(\Omega_1 \setminus \hat{\Omega}_1)^c} dx + \int_{\hat{\Omega}_1 \setminus \Omega_1} G_h * \chi_{(\hat{\Omega}_1 \setminus \Omega_1)^c} dx \right) \\ &\leq \gamma_{LV} |\cos \theta_Y| \left(\int_{\tilde{\Omega}} |D \chi_{(\Omega_1 \setminus \hat{\Omega}_1)}| + \int_{\tilde{\Omega}} |D \chi_{(\hat{\Omega}_1 \setminus \Omega_1)}| \right) \\ &= \gamma_{LV} |\cos \theta_Y| \int_{\tilde{\Omega}} |D \chi_{(\Omega_1 \setminus \hat{\Omega}_1)} - D \chi_{(\hat{\Omega}_1 \setminus \Omega_1)}| = \gamma_{LV} |\cos \theta_Y| \int_{\tilde{\Omega}} |D(u - v)|, \end{aligned}$$

where we have used Lemma 4.2 in last third equation and Lemma 4.1 in the last equation. Therefore, for any ε and u , we choose a neighborhood $\mathcal{N}(u) := \{v \in \mathbb{X}, \|u - v\|_{BV} \leq \frac{\varepsilon}{2\gamma_{LV} |\cos \theta_Y|}\}$ of u . Then for any $v \in \mathcal{N}(u)$, we have

$$|\mathcal{F}_h(v) - \mathcal{F}_h(u)| \leq \frac{\varepsilon}{2}. \tag{59}$$

Combine the above analysis, we have

$$|\mathcal{F}_h(v) - \mathcal{F}(u)| \leq |\mathcal{F}_h(v) - \mathcal{F}_h(u)| + |\mathcal{F}_h(u) - \mathcal{F}(u)| \leq \frac{\varepsilon}{2} + \frac{\varepsilon}{2} = \varepsilon,$$

for any $v \in \mathcal{N}^0(u)$ and $h < h^*$. This finishes the proof. \square

By the Proposition 4.1 and 4.2, we are led to the following Γ -convergence result for the modified functional $\tilde{\mathcal{E}}_h$.

Theorem 4.1. $\tilde{\mathcal{E}}_h(u)$ Γ -converges to $\mathcal{E}(u)$ in \mathbb{X} .

Proof. The basic idea is to use the following property of Γ -convergence (see Proposition 6.20 in [27]) that, if $F_\varepsilon^{(1)}$ Γ -converges to $F^{(1)}$ and $F_\varepsilon^{(2)}$ continuously converges to $F^{(2)}$ in the same topology space, and both $F_\varepsilon^{(2)}$ and $F^{(2)}$ are finite everywhere, then $F_\varepsilon^{(1)} + F_\varepsilon^{(2)}$ Γ -converges to $F^{(1)} + F^{(2)}$.

Notice that $\tilde{\mathcal{E}}_h = (\mathcal{E}_h - \mathcal{F}_h) + \mathcal{F}_{\lambda^2 h}$. By the Propositions 4.1 and 4.2, we use the property twice and the proof is done. \square

5. Numerical experiments

In this section, we use several numerical experiments to illustrate the improvement of the modified algorithm. We implemented the Algorithm 1 in MATLAB installed on a laptop with a 2.7GHz Intel Core i5 processor and 8GB of RAM. The convolutions at the first step in the Algorithm 1 are efficiently evaluated using the fast Fourier transform (FFT).

5.1. Example 1: contact angle in the dynamics

In this example, we check the accuracy of the contact angle when $h_2 = \lambda^2 h_1$ (see (44)) and $h_2 = h_1$ (i.e., original algorithm in [49]). In two cases, we set the equilibrium angle $\theta_Y = \pi/3$ and $\theta_Y = 2\pi/3$ and we get $\lambda = 1.5$. Then, we perform the following experiment when $h_2 = \lambda^2 h_1 = 2.25h_1$ and $h_2 = h_1$ for different values of h_1 :

1. Set the initial condition as a half circle liquid droplet with radius $\pi/2$ on the solid surface, $y = -\pi/2$ (see Fig. 6).
2. Evaluate

$$\phi = \frac{1}{\sqrt{h_1}} G_{h_1} * (\chi_{D_2} - \chi_{D_1}) - \frac{\cos \theta_Y}{\sqrt{h_2}} G_{h_2} * \chi_{D_3}.$$

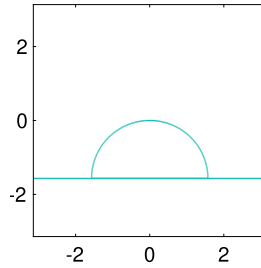


Fig. 6. The half circle initial condition on the solid surface.

Table 1

Errors of the contact angle when $h_2 = 2.25h_1$ and $h_2 = h_1$ with $\theta_Y = \pi/3$ and $h_1 = \pi/128, \pi/256, \pi/512,$ and $\pi/1024$.

h_1	Contact angle when $h_2 = 2.25h_1$	Error	Contact angle when $h_2 = h_1$	Error
$\pi/128$	0.9939	0.0533	0.6630	0.3842
$\pi/256$	1.0098	0.0374	0.6748	0.3724
$\pi/512$	1.0235	0.0237	0.6850	0.3622
$\pi/1024$	1.0399	0.0073	0.6982	0.3490

Table 2

Errors of the contact angle when $h_2 = 2.25h_1$ and $h_2 = h_1$ with $\theta_Y = 2\pi/3$ and $h_1 = \pi/128, \pi/256, \pi/512,$ and $\pi/1024$.

h_1	Contact angle when $h_2 = 2.25h_1$	Error	Contact angle when $h_2 = h_1$	Error
$\pi/128$	2.0628	0.0316	2.4324	0.3380
$\pi/256$	2.0727	0.0217	2.4335	0.3391
$\pi/512$	2.0798	0.0145	2.4289	0.3345
$\pi/1024$	2.0853	0.0091	2.4279	0.3335

3. Use the function named `contour` in Matlab, we find a set of discrete points on the $\delta_{h_{1,2}}^{D_{1,2}}$ -levelset of ϕ . Among these points, find the point $C_1 = (x_1, y_1)$ which is closest to the surface in either the rightmost or leftmost. Then, we find the closest point, $C_2 = (x_2, y_2)$, to C_1 away from the solid surface.

4. Calculate $\theta = \arctan(\frac{y_2 - y_1}{x_2 - x_1})$.

In Table 1, we list the errors of the contact angle when $h_2 = 2.25h_1$ and $h_2 = h_1$ with $\theta_Y = \pi/3$ and $h_1 = \pi/128, \pi/256, \pi/512,$ and $\pi/1024$, separately. When $h_2 = 2.25h_1$, it is obvious to see that the angle converges to $\pi/3 \approx 1.04720$ when we decrease the value of h_1 . However, when $h_2 = h_1$, the angle converges to an incorrect angle. Interestingly, we note that the angles are close to $\pi/4 \approx 0.78540$ which is consistent with the results in (45) and Fig. 4.

In Table 2, we list the errors of the contact angle when $h_2 = 2.25h_1$ and $h_2 = h_1$ with $\theta_Y = 2\pi/3$ and $h_1 = \pi/128, \pi/256, \pi/512,$ and $\pi/1024$, separately. Again, when $h_2 = 2.25h_1$, the contact angle converges to $2\pi/3 \approx 2.09440$. When $h_2 = h_1$, the angle seems to converge to an incorrect angle which is close to $3\pi/4 \approx 2.35619$ showed in (45) and Fig. 4.

In both numerical experiments, we use 4096×4096 grid points to discretize the computational domain $[-\pi, \pi] \times [-\pi, \pi]$.

5.2. Example 2: contact angle in the equilibrium state of the solid wetting problem

In this example, we check the accuracy of the contact angle for the equilibrium state. We apply the adaptive in time strategy proposed in [49] on Algorithm 1 to get the equilibrium state when $\theta_Y = \pi/3$ and $2\pi/3$ on discretized grids with mesh size $dx = \pi/64, \pi/128, \pi/256,$ and $\pi/512$ when $h_2 = \lambda^2 h_1$ and $h_2 = h_1$, respectively. Here, we choose a relatively large initial $h_1 = 3dx$ since we use the adaptive in time strategy. We refer the details of the adaptive in time strategy to [49]. The convergence criterion is that D_1 doesn't change both between two iteration steps in the current discretization and halving the value of h_1 . Table 3 and 4 list the errors of the contact angle and the CPU time when $h_2 = \lambda^2 h_1$ and $h_2 = h_1$ with the equilibrium angle $\theta_Y = 2\pi/3$ and $\pi/3$. In both cases, $\lambda = 1.5$. Obviously, from both tables, the angles converge to the corresponding expected angles θ_Y when $h_2 = 2.25h_1$ while the angles deviate from the correct angles when $h_2 = h_1$.

5.3. Example 3: contact angle hysteresis on a rough surface

In this section, we compare the improved algorithm to the original algorithm [49] in the simulation of the contact angle hysteresis on geometrically rough surfaces. When a droplet spreads on a rough surface, the contact angle can take a range

Table 3

Errors of the contact angle at equilibrium state when $h_2 = 2.25h_1$ and $h_2 = h_1$ with $\theta_Y = \pi/3$.

dx	Initial h_1	Contact angle when $h_2 = 2.25h_1$	Error	CPU time (seconds)	Contact angle when $h_2 = h_1$	Error	CPU time (seconds)
$\pi/64$	$3\pi/64$	0.8004	0.2468	0.07	0.7100	0.3372	0.25
$\pi/128$	$3\pi/128$	0.8570	0.1902	0.59	0.6614	0.3858	0.59
$\pi/256$	$3\pi/256$	0.9960	0.0512	5.5	0.6244	0.4228	5.9
$\pi/512$	$3\pi/512$	1.0227	0.0245	43.2	0.6053	0.4419	43.6

Table 4

Errors of the contact angle at equilibrium state when $h_2 = 2.25h_1$ and $h_2 = h_1$ with $\theta_Y = 2\pi/3$.

dx	Initial h_1	Contact angle when $h_2 = 2.25h_1$	Error	CPU time (seconds)	Contact angle when $h_2 = h_1$	Error	CPU time (seconds)
$\pi/64$	$3\pi/64$	1.8127	0.2817	0.08	2.2554	0.1610	0.11
$\pi/128$	$3\pi/128$	1.9232	0.1712	0.58	2.4058	0.3114	0.52
$\pi/256$	$3\pi/256$	2.0205	0.0739	4.8	2.4995	0.4051	4.8
$\pi/512$	$3\pi/512$	2.1225	0.0281	43.5	2.5247	0.4303	42.2

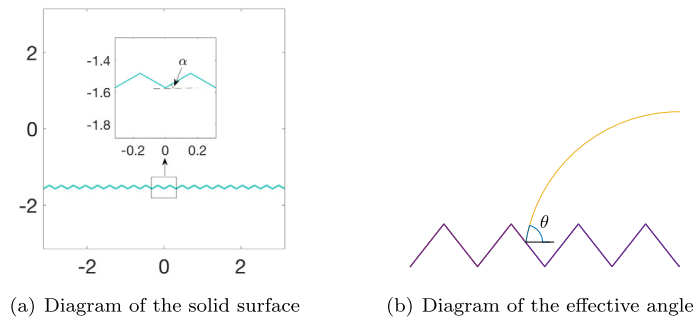


Fig. 7. Diagrams of the solid surface and the effective angle.

of values. The highest (lowest) stable contact angle is termed the advancing (receding) angle Θ_a (Θ_r). The contact angle hysteresis $\Delta\Theta = \Theta_a - \Theta_r$ is an important quantity and determines many properties of the rough surface. To simulate the hysteresis process, we consider the quasi-static spreading of a drop as volume of the drop is gradually increased (advancing) or decreased (receding). We compute the equilibrium state of the drop after liquid is added or extracted in each time step. Theoretically, in each period, when the volume of the droplet is increasing (decreasing) gradually, the apparent contact angle should be approaching to the advancing (receding) angle.

In this experiment, the computational domain is $[-\pi, \pi] \times [-\pi, \pi]$, and the solid surface of is then given by a sawtooth function

$$y = -\frac{\pi}{2} + \frac{\pi \tan(\alpha)}{2k} s(2kx)$$

where $s(x)$ is a sawtooth periodic function with period 2π defined as

$$s(x) = \begin{cases} -1 - \frac{x-\pi}{\pi} & -\pi \leq x \leq 0; \\ \frac{x}{\pi} & 0 < x \leq \pi, \end{cases}$$

α is the angle between solid surface and horizontal direction, and $2k$ denotes the number of the period of the sawtooth on the solid surface (see Fig. 7 (a) for an example when $k = 10$ and $\alpha = \pi/6$). For a rough surface, it is more meaningful to see how the effective contact angle behaves when the volume of the drop is increased or decreased [6]. The effective contact angle is defined as the angle between the contact line and the horizontal surface (see Fig. 7 (b)). The computational domain $[-\pi, \pi] \times [-\pi, \pi]$ is discretized by 4096×4096 grid points and the initial time step is $h_1 = \frac{\pi}{2048}$.

Fig. 8 displays the behavior of the effective contact angle when $k = 10$, $\alpha = \frac{\pi}{6}$. In this case, the Young's angle of the solid surface is $\theta_Y = \frac{\pi}{3}$, the theoretical advancing angle is $\pi/3 + \pi/6 = \pi/2$ and the theoretical receding angle is $\pi/3 - \pi/6 = \pi/6$. In Fig. 8, we use solid lines to denote the line of the theoretic advancing angle and the theoretic receding angle. The results show significant improvement of hysteresis behavior obtained by the new algorithm.

The red dashed line represents the behavior of advancing angle when we increase the volume gradually from 0.2 to 8 and the blue dashed line represents the behavior of the receding angle when we decrease the volume gradually from 8 to 0.2 using the improved threshold dynamics method proposed. In the first figure of Fig. 8, when the volume of the droplet is increasing (decreasing) gradually, we see that in each period, the apparent contact angle is approaching to the advancing (receding) angle accordingly. It matches the theoretic results well.

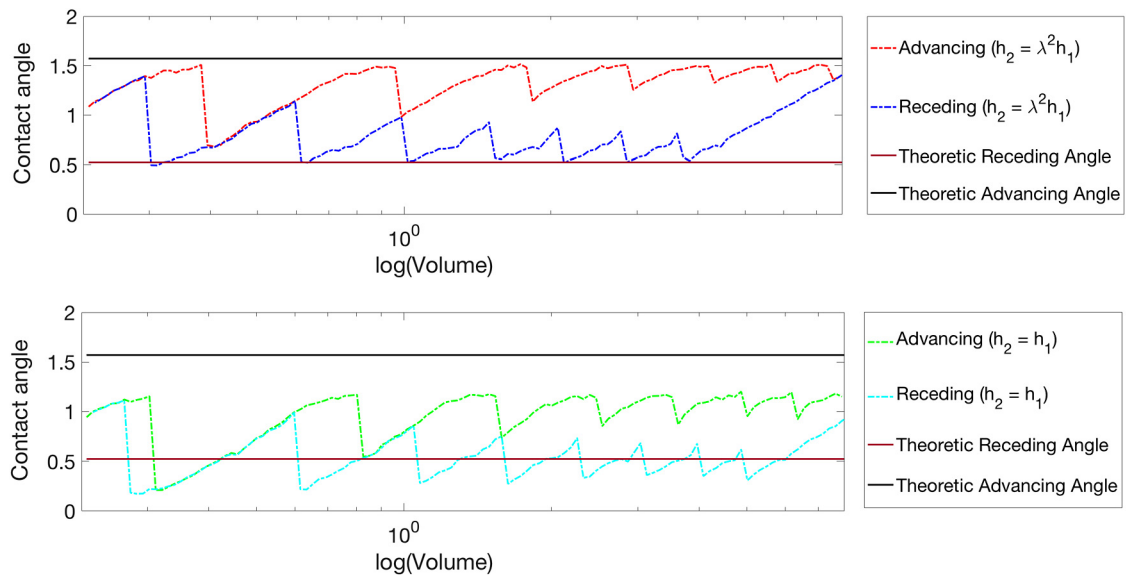


Fig. 8. Advancing and receding contact angles for rough surfaces with $\theta_Y = \pi/3$ and $k = 10$ when $h_2 = \lambda^2 h_1$ and $h_2 = h_1$, separately. (For interpretation of the colors in the figure(s), the reader is referred to the web version of this article.)

However, if we use the original algorithm (i.e., $h_2 = h_1$) to add volume gradually from 0.2 to 8 and then decrease from 8 to 0.2, the results are displayed by the green dashed line and the light blue dashed line in the second figure of Fig. 8. When the volume of the droplet is increasing (decreasing) gradually, we see that in every period, the apparent contact angle is approaching to an incorrect advancing (receding) angle. They deviate from the theoretic result a lot. In fact, the advancing angle is close to $\pi/4 + \pi/6 = 5\pi/12$ and the receding angle is close to $\pi/4 - \pi/6 = \pi/12$. This observation is also consistent with the asymptotic results in (45) and Fig. 4.

6. Conclusions and future work

In this paper, we developed a modified threshold dynamics method for wetting dynamics. The method is simple, efficient, and unconditionally stable. We showed that the contact angle is consistent with the Young's angle and the dynamics at the contact point is consistent with the dynamics of the interface away from the contact point. We extended the analysis in [13] to prove the modified functional Γ -converges to the original functional. We used some numerical examples to verify the improvement of the modified method comparing to the method in [49].

Acknowledgements

This research was supported in part by the Hong Kong Research Grants Council (GRF grants 16302715, 16324416, 16303318 and NSFC-RGC joint research grant N-HKUST620/15). X. Xu also acknowledges the support of NSFC projects 11571354 and 91630208.

References

- [1] G. Alberti, G. Bellettini, A non-local anisotropic model for phase transitions: asymptotic behaviour of rescaled energies, *Eur. J. Appl. Math.* 9 (03) (1998) 261–284.
- [2] G. Alberti, A. DeSimone, Wetting of rough surfaces: a homogenization approach, *Proc. R. Soc. A* 451 (2005) 79–97.
- [3] G. Barles, C. Georgelin, A simple proof of convergence for an approximation scheme for computing motions by mean curvature, *SIAM J. Numer. Anal.* 32 (2) (1995) 484–500.
- [4] E. Bonnetier, E. Bretin, A. Chambolle, Consistency result for a non monotone scheme for anisotropic mean curvature flow, arXiv:1005.4794, 2010.
- [5] A. Chambolle, M. Novaga, Convergence of an algorithm for the anisotropic and crystalline mean curvature flow, *SIAM J. Math. Anal.* 37 (6) (2006) 1978–1987.
- [6] X. Chen, X.-P. Wang, X. Xu, Effective contact angle for rough boundary, *Physica D* 242 (2013) 54–64.
- [7] R. Cox, The dynamics of the spreading of liquids on a solid surface. Part 1. Viscous flow, *J. Fluid Mech.* 168 (1986) 169–194.
- [8] A. Dutt, V. Rokhlin, Fast Fourier transforms for nonequispaced data, *SIAM J. Sci. Comput.* 14 (1993) 1368–1393.
- [9] C.M. Elliott, V. Styles, Computations of bidirectional grain boundary dynamics in thin metallic films, *J. Comput. Phys.* 187 (2) (2003) 524–543.
- [10] M. Elsey, S. Eshedoglu, Threshold dynamics for anisotropic surface energies, *Math. Comp.* 87 (2018) 1721–1756, <https://doi.org/10.1090/mcom/3268>.
- [11] H.Y. Erbil, The debate on the dependence of apparent contact angles on drop contact area or three-phase contact line: a review, *Surf. Sci. Rep.* 69 (4) (2014) 325–365.
- [12] S. Eshedog, Y.-H.R. Tsai, et al., Threshold dynamics for the piecewise constant Mumford–Shah functional, *J. Comput. Phys.* 211 (1) (2006) 367–384.
- [13] S. Eshedoglu, F. Otto, Threshold dynamics for networks with arbitrary surface tensions, *Commun. Pure Appl. Math.* (2015).

- [14] S. Esedoglu, S. Ruuth, R. Tsai, Threshold dynamics for high order geometric motions, *Interfaces Free Bound.* 10 (3) (2008) 263–282.
- [15] L.C. Evans, Convergence of an algorithm for mean curvature motion, *Indiana Math. J.* 42 (2) (1993) 533–557.
- [16] C.W. Extrand, Model for contact angles and hysteresis on rough and ultraphobic surfaces, *Langmuir* 18 (2002) 7991–7999.
- [17] M. Gao, X. Wang, A gradient stable scheme for a phase field model for the moving contact line problem, *J. Comput. Phys.* 231 (2012) 1372–1386.
- [18] K. Ishii, Optimal rate of convergence of the Bence–Merriman–Osher algorithm for motion by mean curvature, *SIAM J. Math. Anal.* 37 (3) (2005) 841–866.
- [19] M. Jacobs, E. Merkurjev, S. Esedoglu, Auction dynamics: a volume constrained MBO scheme, *J. Comput. Phys.* 354 (2018) 288–310, <https://doi.org/10.1016/j.jcp.2017.10.036>.
- [20] S. Jiang, D. Wang, X.-P. Wang, An efficient boundary integral scheme for the MBO threshold dynamics method via NUFFT, *J. Sci. Comput.* 74 (1) (2018) 474–490, <https://doi.org/10.1007/s10915-017-0448-1>.
- [21] C. Kublik, S. Esedoglu, J.A. Fessler, Algorithms for area preserving flows, *SIAM J. Sci. Comput.* 33 (5) (2011) 2382–2401.
- [22] T. Laux, F. Otto, Convergence of the thresholding scheme for multi-phase mean-curvature flow, [arXiv:1602.05857](https://arxiv.org/abs/1602.05857), 2016.
- [23] T. Laux, D. Swartz, Convergence of thresholding schemes incorporating bulk effects, [arXiv:1601.02467](https://arxiv.org/abs/1601.02467), 2016.
- [24] J.Y. Lee, L. Greengard, The type 3 nonuniform FFT and its applications, *J. Comput. Phys.* 206 (2005) 1–5.
- [25] S. Leung, H. Zhao, A grid based particle method for moving interface problems, *J. Comput. Phys.* 228 (8) (2009) 2993–3024.
- [26] P. Mascarenhas, *Diffusion Generated Motion by Mean Curvature*, Department of Mathematics, University of California, Los Angeles, 1992.
- [27] G.D. Maso, *An Introduction to Gamma Convergence*, Birkhäuser, Boston, 1993.
- [28] E. Merkurjev, T. Kostic, A.L. Bertozzi, An MBO scheme on graphs for classification and image processing, *SIAM J. Imaging Sci.* 6 (4) (2013) 1903–1930.
- [29] B. Merriman, J.K. Bence, S. Osher, *Diffusion Generated Motion by Mean Curvature*, UCLA CAM Report 92-18, 1992.
- [30] B. Merriman, J.K. Bence, S.J. Osher, Motion of multiple junctions: a level set approach, *J. Comput. Phys.* 112 (2) (1994) 334–363.
- [31] B. Merriman, S.J. Ruuth, Convolution-generated motion and generalized Huygens' principles for interface motion, *SIAM J. Appl. Math.* 60 (3) (2000) 868–890.
- [32] M. Miranda, D. Pallara, F. Paronetto, M. Preunkert, Short-time heat flow and functions of bounded variation in \mathbb{R}^n , in: *Annales-Faculte des Sciences Toulouse Mathematiques*, vol. 16, Université Paul Sabatier, 2007, p. 125.
- [33] B. Osting, D. Wang, A generalized mbo diffusion generated motion for orthogonal matrix-valued fields, [arXiv:1711.01365](https://arxiv.org/abs/1711.01365), 2017.
- [34] B. Osting, D. Wang, Diffusion generated methods for denoising target-valued images, [arXiv:1806.06956](https://arxiv.org/abs/1806.06956), 2018.
- [35] D. Quere, Wetting and roughness, *Annu. Rev. Mater. Res.* 38 (2008) 71–99.
- [36] W. Ren, P.H. Trinh, E. Weinan, On the distinguished limits of the Navier slip model of the moving contact line problem, *J. Fluid Mech.* 772 (2015) 107–126.
- [37] S.J. Ruuth, A diffusion-generated approach to multiphase motion, *J. Comput. Phys.* 145 (1) (1998) 166–192.
- [38] S.J. Ruuth, Efficient algorithms for diffusion-generated motion by mean curvature, *J. Comput. Phys.* 144 (2) (1998) 603–625.
- [39] S.J. Ruuth, B. Merriman, Convolution-thresholding methods for interface motion, *J. Comput. Phys.* 169 (2) (2001) 678–707.
- [40] S.J. Ruuth, B.T. Wetton, A simple scheme for volume-preserving motion by mean curvature, *J. Sci. Comput.* 19 (1–3) (2003) 373–384.
- [41] K. Svadlenka, E. Ginder, S. Omata, A variational method for multiphase volume-preserving interface motions, *J. Comput. Appl. Math.* 257 (2014) 157–179.
- [42] D. Swartz, N.K. Yip, Convergence of diffusion generated motion to motion by mean curvature, [arXiv:1703.06519](https://arxiv.org/abs/1703.06519), 2017.
- [43] R. Viertel, B. Osting, An approach to quad meshing based on harmonic cross-valued maps and the Ginzburg–Landau theory, [arXiv:1708.02316](https://arxiv.org/abs/1708.02316), 2017.
- [44] D. Wang, A. Cherkhev, B. Osting, Dynamics and stationary configurations of heterogeneous foams, [arXiv:1811.03570](https://arxiv.org/abs/1811.03570), 2018.
- [45] D. Wang, H. Li, X. Wei, X.-P. Wang, An efficient iterative thresholding method for image segmentation, *J. Comput. Phys.* 350 (2017) 657–667.
- [46] D. Wang, B. Osting, A diffusion generated method for computing Dirichlet partitions, [arXiv:1802.02682](https://arxiv.org/abs/1802.02682), 2018.
- [47] D. Wang, B. Osting, X.-P. Wang, *Interface dynamics for an Allen–Cahn-type equation governing a matrix-valued field*, submitted, 2019.
- [48] D.E. Womble, A front-tracking method for multiphase free boundary problems, *SIAM J. Numer. Anal.* 26 (2) (1989) 380–396.
- [49] X. Xu, D. Wang, X.-P. Wang, An efficient threshold dynamics method for wetting on rough surfaces, *J. Comput. Phys.* 330 (2017) 510–528.
- [50] X. Xu, X.P. Wang, The modified Cassie's equation and contact angle hysteresis, *Colloid Polym. Sci.* 291 (2013) 299–306.
- [51] T. Young, An essay on the cohesion of fluids, *Philos. Trans. R. Soc. Lond.* 95 (1805) 65–87.
- [52] H. Zhao, T. Chan, B. Merriman, S.J. Osher, A variational level set approach to multiphase motion, *J. Comput. Phys.* 127 (1) (1996) 179–195.